Monthly North Atlantic Sea Level Pressure reconstruction back to 1750 CE using Artificial Intelligence optimization

Fernando Jaume-Santero*

Departamento de Ciencias de la Tierra y Astrofísica, Facultad de Ciencias Físicas, Universidad Complutense de Madrid, Madrid, Spain and Instituto de Geociencias (IGEO), CSIC-UCM, Madrid, Spain

David Barriopedro

Instituto de Geociencias (IGEO), CSIC-UCM, Madrid, Spain

Ricardo García-Herrera

Departamento de Ciencias de la Tierra y Astrofísica, Facultad de Ciencias Físicas, Universidad Complutense de Madrid, Madrid, Spain and Instituto de Geociencias (IGEO), CSIC-UCM, Madrid, Spain

Jürg Luterbacher

Science and Innovation Department, World Meteorological Organization (WMO), Geneva, Switzerland

Corresponding author: Fernando Jaume-Santero, fjaume@ucm.es

ABSTRACT

Main modes of atmospheric variability exert a significant influence on weather and climate at local and regional scales on all time scales. However, their past changes and variability over the instrumental record are not well constrained due to limited availability of observations, particularly over the oceans. Here we couple a reconstruction method with an evolutionary algorithm to yield a new $1^\circ \times 1^\circ$ optimized reconstruction of monthly North Atlantic sea level pressure since 1750 from a network of meteorological land and ocean observations. Our biologically-inspired optimization technique finds an optimal set of weights for the observing network that maximizes the reconstruction skill of sea level pressure fields over the North Atlantic Ocean, bringing significant improvements over poorly sampled oceanic regions, as compared to non-optimized reconstructions. It also reproduces realistic variations of regional climate patterns such as the winter North Atlantic Oscillation and the associated variability of the subtropical North Atlantic high and the subpolar low pressure system, including the unprecedented strengthening of the Azores High in the second half of the twentieth century. We find that differences in the winter North Atlantic Oscillation indices are partially explained by disparities on estimates of its Azores High center. Moreover, our reconstruction also shows that displacements of the summer Azores High center towards the northeast coincided with extremely warm events in western Europe including the anomalous summer of 1783. Overall, our results highlight the importance of improving the characterization of the Azores High for understanding the climate of the Euro-Atlantic sector and the added value of artificial intelligence in this avenue.

1. Introduction

Atmospheric conditions are nowadays continuously monitored by near-surface and remote-sensing instruments that help improve our understanding of Earth's climate system. However, climate information from instrumental records drastically decreases the further we go back in time, leading to a problem of data scarcity, particularly acute in the pre-industrial era (before 1850 of the Common Era, CE), important land areas in the Southern Hemisphere and Eurasia, as well as in the oceans (Christensen et al. 2013). This hampers the characterization of the climate system, its internal variability, and responses to external forcings, even in regions with the largest amount of historical observations such as Europe (Küttel et al. 2010; Cram et al. 2015; Franke et al. 2017; Brönnimann et al. 2020; Noone et al. 2020). The limited amount of information over the North Atlantic ocean, makes it difficult to fully characterize the North Atlantic Oscillation (NAO), the leading mode of atmospheric variability over the North Atlantic, which is dominated by the meridional rearrangement of sea level pressure (SLP) anomalies between subtropical and subpolar latitudes (e.g., Hurrell and Deser (2010) and references therein). The NAO pattern (more discernible during winter season) involves changes in two semi-permanent action centers, the subpolar Icelandic low pressure system (IL) (Hordon 1987; Sahsamanoglou 1990) and the subtropical Azores High (AH) associated with the descending branch of the Hadley Cell over the Atlantic Ocean (Zishka and Smith 1980; Davis et al. 1997; Iqbal et al. 2019).

Alternating phases of the winter NAO generate strong changes in surface temperatures, wind, and precipitation over the Atlantic region and its surroundings (e.g., Trigo et al. 2004). When the aforementioned action centers are stronger than average (i.e., NAO's phase is positive), the pressure gradient between them becomes more intense, and the storm tracks shift towards

higher latitudes, therefore increasing precipitation and temperatures over parts of northern Europe whereas the southern regions experience reduced precipitation rates (e.g., Hurrell and Deser 2010). Historical timeseries of the NAO are generated using sets of instrumental observations over different locations in Europe, Greenland and North America (Cook et al. 2019), which can be extended further back in time with proxy-based reconstructions (e.g., Luterbacher et al. 1999, 2001; Ortega et al. 2015; Cook et al. 2019; Hernández et al. 2020). Although several instrumental-based NAO indices have been published in the past (e.g., Hurrell 1995; Jones et al. 1997; Luterbacher et al. 1999, 2001; Vinther et al. 2003), they show discrepancies particularly prior to the 19th century, when the number and spatial coverage of observations is the lowest (e.g., Luterbacher et al. 1999; Schmutz et al. 2000; Luterbacher et al. 2001; Cook et al. 2019; Hernández et al. 2020). These differences hamper the study of past changes in the NAO and their causes, ultimately limiting the quantification of internal variability and externally forced responses of the atmospheric circulation (e.g., Pinto and Raible 2012; Christensen et al. 2013, and references therein).

In summer, the NAO pattern is different from the canonical pattern observed in the remainder part of the year and does not involve changes in the AH, showing variability centers over Greenland and the UK, instead (e.g., Folland et al. 2009). The associated impacts are also different, modulating temperature and precipitation conditions over northwestern and southeastern Europe (e.g., Bladé et al. 2012). Being detached from the summer NAO, the summer AH still experiences changes in intensity, location and spatial extent with strong influence in the climate conditions of southwestern Europe and North America (e.g., Davis et al. 1997; Falarz 2019). As these fluctuations cannot be fully captured by land observations or inferred from teleconnections with other actions centers affecting continental areas (e.g., IL), past changes in the summer AH remain poorly constrained before the 20th century (e.g., Davis et al. 1997; Küttel

et al. 2010). Current knowledge on the historical evolution of AH mainly relies on SLP field reconstructions from observations that use reduced-space optimal interpolation techniques to fill the gaps (e.g., Luterbacher et al. 2002; Allan and Ansell 2006; Casty et al. 2007; Küttel et al. 2010), or hybrid products such as reanalyses (Srivastava et al. 2012; Cherchi et al. 2018; Iqbal et al. 2019) that benefit from the physical consistency of models to generate spatially-resolved history fields. Although important efforts have been made to retrieve high quality marine climate data (e.g., Freeman et al. 2017; García-Herrera et al. 2018), most SLP observations still come from land-based stations (Cram et al. 2015; Noone et al. 2020), with reduced ability to capture realistic changes in atmospheric variability over the oceans (Küttel et al. 2010). This highlights the importance of developing more sophisticated techniques to improve the reconstruction skill over regions with a lack of climate data (e.g., North Atlantic ocean), and extract strategic information on the main patterns of climate variability such as the NAO in winter and the AH in summer.

Within this context, new methods that maximize the extraction of information from climate datasets have recently emerged as promising tools to reconstruct spatial fields, while preserving major features of the variability (Carro-Calvo et al. 2020; Kadow et al. 2020; Vaccaro et al. 2021). Joining statistics and computer science, artificial intelligence (AI) is a multidisciplinary field with different areas of expertise such as machine learning (LeCun et al. 2015; Kadow et al. 2020), and optimization (Swarnkar and Swarnkar 2019; Soto et al. 2019). Regarding the latter, some optimization techniques (Vrugt and Robinson 2007; Eiben and Smith 2015) have been used in Earth and environmental sciences to improve solar and wind power forecasts at local scales (Salcedo-Sanz et al. 2018), fill the gaps in observational datasets (Kadow et al. 2020) or maximize the skill of climate field reconstructions (CFR) (Salcedo-Sanz et al. 2019; Jaume-Santero et al. 2020). In particular, evolutionary algorithms (inspired by natural selection

processes) provide optimized solutions for high dimensional non-linear problems (Vrugt and Robinson 2007; Eiben and Smith 2015), including those in climate science (Salcedo-Sanz et al. 2019). When combined with traditional methods, they are effective in the task of increasing the reconstruction skill of thermodynamic fields such as temperature (Salcedo-Sanz et al. 2019; Jaume-Santero et al. 2020), and dynamic fields such as wind speed (Salcedo-Sanz et al. 2018), by performing an optimized selection of records from the available observing network.

Here we couple an evolutionary algorithm with a CFR method to obtain a high-resolution reconstruction ($1^\circ \times 1^\circ$) of monthly SLP fields over the North Atlantic for 1750-2004 from historical land-based observations over Europe, Greenland and North America. In terms of spatial coverage, resolution and number of observations, this new monthly SLP dataset supersedes the statistically-derived seasonal SLP datasets of Luterbacher et al. (2002) and Küttel et al. (2010). More importantly and as the main novelty of this study, we apply an evolutionary AI-based method specially designed to optimize the information contained in networks with a low number of station observations. Different to the aforementioned applications of evolutionary algorithms, the observing network employed herein is affected by limited data availability (incomplete time series), which represents an additional constraint. The evolutionary algorithm is designed to find an optimized combination of weights for the observing network that maximizes the reconstruction skill of the SLP field. The reconstruction performance is compared against reconstructions generated with the same set of observations but without optimization, and allows us to describe the atmospheric climate variability of the North Atlantic sector for the past 255 years focusing on major seasonal features such as the winter NAO and the summer AH.

2. Data description

Two observational-based datasets have been used for the reconstruction. The first one is the largest currently available network of quality-checked SLP observations from Luterbacher et al. (2002) and Küttel et al. (2010). It consists of 121 monthly series of SLP with different time lengths within the 1750-2004 period and distributed over the east coast of North America, Greenland and Europe. In comparison with Luterbacher et al. (2002) and Küttel et al. (2010) we have used a few additional long series from North America and Europe (see Cram et al. 2015; Noone et al. 2020, for details). The number and coverage of observations (Fig. 1) increases with time, being the largest over the 1875-1975 period (up to more than 100 simultaneous observations). However, there are no more than 23 simultaneous observations from 1750 to 1835 CE, and this pronounced decrease in data availability is accompanied by changes in spatial coverage, which is restricted to Europe.

The second dataset is the monthly SLP field of the NOAA-CIRES-DOE 20th Century Reanalysis V3 (20CRv3, hereafter) (Slivinski et al. 2019) which is provided in a $1^\circ \times 1^\circ$ grid from 1836 to 2014 CE. The reanalysis assimilates observations of surface pressure and prescribes sea surface temperatures and sea ice distribution to yield the 3-D state of the atmosphere. The 20CRv3 reanalysis provides complete information in space and time and is used to reconstruct the spatially resolved SLP field over the North Atlantic ([20°N -73°N], [95°W - 50°E]; the predictands) from the subset of observations that are available for each month of the 1750 - 2004 period (the predictor), as well as to assess the reconstruction's performance for the optimization process (more details in the methodology section). The 20CRv3 was preferred to purely instrumental products because it provides the longest period of continuous data, with full spatial coverage, high

resolution and model-based physical consistency.

After testing the consistency of the two datasets, only 101 instrumental series were employed in the reconstruction, discarding stations that were too close (embedded in the same $1^\circ \times 1^\circ$ grid point of the reanalysis) or significantly biased with respect to the closest grid point series of the reanalysis during the 1836-2004 period (most of them at high altitudes over the Alps). Despite the presence of errors in both datasets, the combined use of instrumental and reanalyzed observations through artificial intelligence can help uncover spatial patterns by exploiting robust relationships between the local series and the large-scale field, as also shown for other observational datasets (e.g., Kadow et al. 2020) and fields with General Circulation Models (Barnes et al. 2019). These relationships are herein summarized as a set of local weights for the observing network, which are retrieved by the CRO optimization and subsequently applied to the predictors during the reconstruction process.

To verify that the results of the optimization are robust with respect to the datasets employed and not mere statistical artefacts, we also performed a model-based sensitivity experiment with historical and past1000 simulations from CMIP6-PMIP4 (Eyring et al. 2016; Jungclaus et al. 2017). Both simulations are fully-forced with standard forcing datasets following the specifications included in the input4MIPs documentation (http://goo.gl/r8up31). As the optimization process is time-consuming, a multi-model ensemble was not affordable. Therefore, as a testbed, we used the MRI-ESM2-0 model (Yukimoto et al. 2019), whose spatial resolution (1°) is similar to that of the 20CRv3. Moreover, model outputs were regridded to the reanalysis' grid using a bilinear interpolation method. In this experiment, we selected the simulated SLP series from 1750 to 1835 of the model grid points that contain the observed records to create pseudo-observations mimicking the characteristics of the observing network (i.e, spatial

distribution and missing data), and used them to reconstruct the simulated SLP fields of the model. Similar experiments involving pseudo-observations for General Circulation Model simulations have already been employed to assess the performance of different reconstruction methodologies within the controlled environment of the model world, where the state of the surrogated climate system is well constrained (e.g., Smerdon 2011; Jaume-Santero et al. 2020). This allows us to estimate the potential influence of observational biases on the reconstruction skill.

To further test the performance of the reconstruction, we have also employed observational-based SLP datasets, such as HadSLP2 (1850-2004, Allan and Ansell 2006) and NCAR SLP (1899-2019, Hurrell et al. 2020), previous SLP reconstructions (1750-1886, Küttel et al. 2010), as well as European temperature reconstructions (1500-2003, Luterbacher et al. 2004), and a suite of instrumental-based NAO indices, which will be further described in the corresponding section of the results.

3. Methodology

In this study, a novel hybrid reconstruction approach was adopted, by coupling a CFR technique, the Analogue Method (AM) (Gómez-Navarro et al. 2017) with an evolutionary algorithm, the Coral Reef Optimization (CRO) algorithm (Salcedo-Sanz 2017).

This approach has also been successfully employed in pseudo-proxy reconstructions of global temperature from a spatially-biased distribution of perfect records taken from a model ensemble (Jaume-Santero et al. 2020). However, it has not been applied to fields other than temperature or to real observations, which are affected by additional sources of uncertainty such as observational errors and gaps in data availability. Similar to other CFR techniques, the AM reconstruction

provides the spatially-resolved monthly SLP field over the North Atlantic (the predictand) using as predictors the available SLP observations of the observing network for each month of the 1750-2004 period (Fig. 2). In this standard approach, all available records contribute equally during the reconstruction process. However, Jaume-Santero et al. (2020) found that wisely selected subsets of predictors can improve the reconstruction skill retrieved from the full network by minimizing the spatial bias associated with the non-homogenenous distribution of records. This optimized selection is equivalent to imposing a binary set of weights to the observing network, depending on whether the record is employed (1) or not (0) for the reconstruction. The CRO algorithm is herein employed to derive an optimized set of weights to the available network of SLP observations as illustrated in Fig. 2. Instead of selecting / rejecting predictors, as in Jaume-Santero et al. (2020), a more efficient approach is implemented here, which exploits and optimizes the information of all records by assigning non-discrete weights (ranging from 0 to 1) to the observing network. These optimized weights are subsequently imposed in the AM reconstruction, yielding a CRO-AM optimized reconstruction of the SLP field over the North Atlantic (Fig. 2). To quantify the effect of weighting, we compare the monthly North Atlantic SLP reconstructions obtained with and without optimization of the observing network, as provided by the CRO-AM and AM, respectively. In both cases, the performance of the SLP field reconstruction is assessed with respect to the 20CRv3 reanalysis, which is also employed for the reconstruction and optimization steps, as explained in the following subsections.

a. The Analogue Method

The AM reconstructs an unknown target field $\mathbf{Z}(t)$ at time t from a concurrent set of predictors $\mathbf{X}(t)$ by searching for analogues of the predictor vector within a reference dataset $\mathbf{Y}$ with complete

information of the target field over a given time interval (e.g., Lorenz 1969; Graham et al. 2011; Franke et al. 2011; Gómez-Navarro et al. 2015; Talento et al. 2019; Bothe and Zorita 2020). AM reconstructions do not require calibration (explicit relationships between the predictors and the predictand) or an independent period of validation, but a large pool of spatially resolved fields in the reference dataset to guarantee a sufficient number of analogues (Gómez-Navarro et al. 2015). Herein, the monthly SLP fields of the 20CRv3 reanalysis over the 1836-2014 period are used as a pool $\mathbf{Y}$ to search for analogues of the SLP observations (the predictors, $\mathbf{X}(\mathbf{t})$), from which the spatially resolved SLP field over the North Atlantic (the predictand, $\mathbf{Z}(\mathbf{t})$) can be reconstructed. For a given month, t_k, of the 1750-2004 period with predictors $\mathbf{X}(t_k)$, analogues are determined by calculating the distance, dist $(\mathbf{Y},\ \mathbf{X}(t_k))$ for all months $t_i \neq t_k$ of the pool $\mathbf{Y}$ (i.e., the 1836-2004 SLP fields of the 20CRv3 reanalysis excluding the month that we intend to reconstruct). For each t_i, the distance is measured as the ℓ_2 norm of the SLP values over the p predictors available at time t_k,

$$\|\mathbf{Y}(t_i) - \mathbf{X}(t_k)\|^2 = \sum_{j=1}^{p} \left[y_j(t_i) - x_j(t_k)\right]^2 \quad t_i = t_1, \ldots, t_k - 1, t_k + 1, \ldots, t_m \tag{1}$$

where x_j is the SLP observation of the predictor j, y_j is the SLP value in the corresponding grid point of reference dataset $\mathbf{Y}$, and m is the size of the pool (a total of 2,160 monthly maps). Note that in Eq. 1, $\mathbf{Y}(t_i)$ vectors are restricted to the predicting network (the grid points of the 20CRv3 reanalysis containing the locations of the observations). The N best analogues $n_1, \ldots, n_N$ of $\mathbf{X}(t_k)$ in $\mathbf{Y}$ are identified as those $t_{n_i} \in t_i$ with the lowest Euclidean distance in Eq. 1, i.e., the N maps of the pool with the closest values $\mathbf{Y}(t_i)$ to those of the predicting network $\mathbf{X}(t_k)$. Note that for each analogue t_{n_i} in $\mathbf{Y}$ the spatial information of the SLP field is complete so that the full $\mathbf{Y}(t_{n_i})$ pattern over the North Atlantic represents a possible configuration of the target field compatible with the

state of local predictors. Therefore, the spatial field of the predictand $\mathbf{Z}(t_k)$ is reconstructed as the mean SLP pattern averaged for the N best analogues of $\mathbf{X}(t_k)$ in $\mathbf{Y}$, following Eq. 2,

$$\mathbf{Z}(t_k) = \frac{1}{N}\sum_{i=1}^{N}\mathbf{Y}(t_{n_i}) \tag{2}$$

where $\mathbf{Y}(t_{n_i})$ is the monthly SLP field over the North Atlantic for the analogue t_{n_i} of the reference dataset. Note that in Eq. 2, $\mathbf{Y}(t_{n_i})$ is computed over the entire spatial domain, as opposed to Eq. 1, where $\mathbf{Y}(t_{n_i})$ is restricted to the predicting network. The standard deviation across the N analogues provides a measure of the uncertainty (i.e., how much the large-scale field is constrained by the available set of observations). After testing different N values ranging from 1 to 50, we used the $N = 10$ best analogues of each month. This number was chosen as a balance between two performance metrics of the reconstruction, computed with respect to the 20CRv3 reanalysis over the 1836-2004 period: the Pearson correlation coefficient, which increases with N, and the variability ratio, which decreases with N (Fig. S1).

This AM reconstruction employs the full network of observations, without discrimination among the records, which are considered equally informative (weights of 1). To test the effect of optimizing the observing network, an additional CRO-AM reconstruction was derived by imposing an optimized set of weights provided by the CRO algorithm (see next section) during the AM reconstruction. These weights are used in the computation of the RMSE by replacing the ℓ_2 norm of Eq. 1 with a weighted ℓ_2 norm (Eq. 3), therefore affecting the selection of the best analogues and the reconstructed field:

$$\|\mathbf{Y}(t_i) - \mathbf{X}(t_k)\|_w^2 = \sum_{j=1}^{p} w_j \left[y_j(t_i) - x_(t_k)\right]^2 \quad t_i = t_1, \ldots, t_k - 1, t_k + 1, \ldots, t_m \tag{3}$$

where w_j is the local weight (between 0 and 1) for the predictor j. In that way, the information of the full network is exploited, while acknowledging differences in the predictive skill of individual sites. This approach is novel, and represents an important step with respect to Jaume-Santero et al. (2020), where a subset of optimal locations was selected (weights equal to 1 or 0), therefore discarding observations that could still provide useful information when the availability of the remaining records is compromised.

The performance of the CRO-AM and AM reconstructions, obtained with and without optimized weights, are assessed with respect to the 1836-2004 period of the 20CRv3 reanalysis, allowing us to quantify the improvements of the optimized reconstruction. The skill of the reconstructions is measured with the area-weighted root-mean-squared error (RMSE) of the reconstructed North Atlantic SLP field over the reconstructed period (Fig. 2),

$$\mathrm{RMSE}\left(\mathbf{Z},\mathbf{Y}\right)=\sqrt{\frac{1}{n}\sum_{t=1}^{n}\sum_{j=1}^{h}a_j\left[z_j(t)-y_j(t)\right]^2} \tag{4}$$

where j is the grid cell of the spatial domain (with h grid points), n is the length of the reconstructed period, and a_j is the weight associated with the area of the grid cell j (the cosine of the latitude, divided by the sum of weights over all grid points of the domain, so that weights add 1).

b. The Coral Reef Optimization

The CRO is a meta-heuristic algorithm (Salcedo-Sanz 2017) that emulates the living processes of corals and their evolution within a reef. By limiting the number of corals within the reef, the best adapted species will have a higher probability of surviving, promoting subsequent evolution of the best individuals over the next generations. Mathematically, this is implemented through

different techniques known as search operators such as genetic crossovers (Forrest 1993) that recombine the set of solutions to iteratively generate better solutions. There is also a small probability of spontaneous random perturbations in the set of solutions (known as mutations) to expand the space of solutions. Evolutionary algorithms such as the CRO do not require training over out-of-sample data but an in-sample cost function to minimize. Being optimization methods for high combinatorial problems where there is often no unique solution, they proceed iteratively providing better solutions in each new generation. The reader is referred to Salcedo-Sanz et al. (2019) and references therein for a detailed description of this evolutionary algorithm.

We used the CRO algorithm to find optimized weights for the predicting network, which are later applied during the AM reconstruction (Fig. 2). In this case, different corals represent different sets of weights, which can be interpreted as a measure of the predictive skill of the local records, under the given restrictions of the observing network. For ideally perfect conditions, weights would only depend on the relationships between the local observations and the links of the latter with the target field. However, in the presence of uncertainties contaminating these relationships, weights are also affected by changes in the observing network over the reconstructed period and inconsistencies between the predictors and the target (e.g., observational errors and/or biases in the reanalysis).

In the coupled CRO-AM reconstruction, the reconstruction error (Eq. 4) is the cost function to be minimized by the CRO. This is done by assigning weights w_j to the predicting network (Eq. 3) that improve the overall performance of the reconstruction (Eq. 4). In each generation of this optimization process, the set of weights is refined by the CRO and the cost function is further decreased (as shown in the iterative step of Fig. 2). The CRO-AM reconstruction error shows an asymptotic behaviour with the number of iterations (Fig. S2) so that after 600 generations there is

little improvement, meaning that we are approaching an optimal solution. Therefore, we kept the solutions obtained after 600 iterations of the CRO.

Using this optimization process, weights have been determined for each calendar month separately. Recall that the reconstruction error is evaluated over the 1836-2004 period, for which (the 20CRv3 reanalysis) is available. Therefore, the set of weights and the CRO-AM reconstruction are optimized for the characteristics of the observing network during that time interval. For the remaining period of the reconstruction (1750-1835), one could use the weights of the 1836-2004 interval. However, this approach would not guarantee an optimized reconstruction for the early period, because substantial changes in the predicting network (e.g., the limited temporal availability of records over the eastern North Atlantic; Fig. 1) are expected to affect the distribution of weights. Therefore, the set of monthly weights were optimized separately for 1750-1835. To do this, we took the SLP observations for the 1919-2004 period and constrained them with the same gaps in data availability as in the 1750-1835 interval. Note that these two periods comprise the same number of years, and that the 20CRv3 reanalysis is available for the former, therefore providing the reference field required by the CRO (the cost function is now the reconstruction error of Eq. 4 evaluated over 1919-2004). In that way, weights can be optimized for a network that preserves the spatio-temporal distribution of observations of the early reconstruction period. This set of optimized weights is subsequently applied to the actual observations of 1750-1835 to reconstruct the North Atlantic SLP for this period. This indirect approach assumes that the relationships between the local records and the large-scale field do not change substantially with time, and that temporal changes in dataset errors are not so large as to affect the overall distribution of weights. While these assumptions may not hold for all local records, they were preferred

to more unrealistic approximations that ultimately presume small changes in the observing network.

For the pseudo-reconstructions of the model experiment, we repeated the same process but replacing the SLP observations with the model-based pseudo-observations described in the previous section, and the 20CRv3 reference dataset with the simulated regridded fields. To reproduce the real-world constraints in data availability and uncertainty, we imposed the observed gaps to the pseudo-observations, and perturbed them with white noise so that their signal-to-noise ratio (SNR) equals that between the local observations and the 20CRv3 reanalysis. As an stringent test, AM and CRO-AM pseudo-reconstructions were obtained for the early period (1750-1835), when the predicting network is severely reduced. Note that in this model experiment we have the ground truth information for 1750-1835, allowing us to directly infer the optimized weights of that period. With this experiment we can assess whether the spatial patterns of optimized weights and reconstruction improvement obtained for the early period of observations are also present in the model's world under realistic conditions of the predicting network and despite the presence of model biases.

4. Results

a. Optimized networks

Figure 3 shows the spatial distribution of optimized weights for two representative months of the year and the two considered sub-periods: 1836-2004 (Fig. 3a and b) and 1750-1835 (Fig. 3c and d). Local weights for the earlier reconstruction period are substantially different from their more recent counterparts. Overall, higher weighting values are assigned to the reduced subset of observations of the 1750-1835 period than to the records of the almost complete network of 1836-2004. For instance, around 85% of the October observations from 1836 to 2004 CE

have low weights (below 0.5), whereas this number decreases to 70% for the 1750-1835 period. Therefore, observations gain representativeness when the lack of information increases, and locations with low weights in a large network can be very informative when considering a reduced subset of the network. In spite of this, there are no generalized high weights, even in the case of extreme data scarcity. Indeed, for the earlier reconstruction period, only 7 out of 23 records have weights with values above 0.5. Therefore, the CRO algorithm only assigns high values to a few locations, stressing the advantages of exploiting the information of the full network rather than selecting a subset, particularly when gaps are present. The spatial distribution of weights in the 1836-2004 period is preserved for different months of the year, with higher values for latitudes in-between 30°N and 50°N. However, the pattern of weights changes from one month to another for 1750-1835 (Fig. 3c and d), indicating that a "one-fits-all" pattern of monthly weights can be challenging when there are extensive unsampled areas. It is difficult to determine whether this seasonal cycle stems from climatological aspects that are not evidenced in larger networks or from peculiarities of the limited network of 1750-1835.

Recall that weights apply to an incomplete network of observations, and hence low weights can be caused by poor instrument calibration, reduced data availability of records (especially in key areas such as the North Atlantic Ocean), an overall weak predictive skill or redundant information with respect to that provided by the remaining records. Therefore, inferences of physical links among stations (or between local records and the large-scale flow) based on the detailed distribution of local weights within the network can be misleading and should be interpreted with caution. Note also that although changes in data availability were taken into account in the optimization process, weights are time invariant during each reconstructed period (except for the annual cycle). Strictly speaking, weights are expected to change with

time, following the configuration of the observing network at any time. Optimizing the set of weights for each month of the 1750-2004 period is not necessarily the best strategy, since it would be computationally expensive and makes it difficult to assess in a straightforward way the spatial pattern of weights as well as the reconstruction errors due to changes in data availability. Moreover, this approach is not expected to cause large differences in the optimized weights for relatively small changes in the distribution of records, particularly if the number of observations is large. The pronounced changes in the coverage of observations for the earlier reconstruction period leave large un-sampled areas (e.g., the northern part of the North Atlantic and the east coast of North America) as compared to 1836-2004, justifying a separated optimization.

To further test the robustness of our results, we also performed a CRO-AM reconstruction of the 1919-2004 SLP fields of the 20CRv3 reanalysis by replacing the observations with the closest reanalysis grid point series and imposing the same spatio-temporal availability as in 1750-1835. Grid point series are not perturbed so that they represent perfect local predictors (SNR = ∞) of the 20CRv3 "ground truth". This subset is also less affected by artifacts (e.g., the mismatch of the spatial scales resolved by the reanalysis and the station-based observations) and is more physically consistent with the large-scale field targeted by the reconstruction. The resulting weights for this reanalysis experiment are very similar to those found for the observations (Fig. S3), stressing the coherence of the station-based and reanalysis grid point series. As the SNR is higher in the reanalysis experiment, the overall agreement also suggests a limited influence of local observational errors on the distribution of weights of the observing network. Furthermore, we also find a similar spatial pattern of weights for the model experiment, indicating that the optimization is little affected by the specific realization of internal variability. The model experiment also shows that model biases in the climatology or the simulated responses to external forcings are either small or play

a minor role in the optimized weights. These results, and the overall model agreement with the observed distribution of weights for 1750-1835 lend support to the approach adopted for inferring the optimized weights for that period (Section 3b).

b. Skill of the optimized networks

Figure 4 summarizes the performance of the CRO-AM optimized networks for 1750-1835 and 1836-2004, and compares it to reconstructions obtained with the AM only (i.e., without weighting). The skill is quantified with the area-weighted RMSE of SLP over the North Atlantic, computed with respect to the corresponding validation period of the 20CRv3 reanalysis (1919-2004 and 1836-2004, respectively). The optimized network of the 1750-1835 period yields area-weighted RMSE below 4 hPa all year round, almost doubling the RMSE retrieved with the much denser network of the 1836-2004 period. In both periods, the RMSE displays a pronounced annual cycle with maxima in winter and minima in summer, as expected from the seasonal changes in variability of the North Atlantic atmospheric circulation. On the other hand, the optimized networks have higher skill than their un-weighted counterparts for all months of the year and the two reconstructed periods. This improvement is present for most time steps of the reconstruction as seen in Fig. S4, indicating that the optimization performs well regardless of the number and distribution of observations. For some months the RMSE of the optimized but sparse network of 1750-1835 approaches that of the denser un-weighted network of 1835-2004, which is quite remarkable because the latter has several times more observations than the former. This indicates that optimized networks have measurable effects in the reconstruction skill, which can be compared to those induced by other sources of uncertainty (e.g. data density). For example, the weighting improvement for the sparse networks of the early period is equivalent to that obtained with the un-weighted network after a 2-fold increase in data density. This improvement is

achieved thanks to the optimal weights imposed in the reconstruction method, where analogues are selected to enhance the entire field and not only the grid points with available information (Fig. S5).

Although optimized and non-optimized reconstructions have significant correlations ($p < 0.05$) in both periods (Fig. S6) with the target field, CRO-AM reconstructions perform significantly better than AM reconstructions for most regions, especially over the North Atlantic Ocean and the Canadian North Pole, where Pearson correlation coefficients increase significantly above values obtained without optimization (Fig. 4a and b). The only regions where the reconstruction is not improved by network weighting are those with a higher density of stations (e.g., specific areas of Europe). This indicates that the skill of the AM reconstruction is biased towards well sampled regions, and at the expense of sacrificing its performance over regions with a sparser distribution of observations. Differently, the optimized network maximizes the reconstruction skill of the whole study region, reducing the spatial bias induced by the non-homogeneous and ever-changing distribution of climate records. This is consistent with previous findings indicating improved pseudo-proxy reconstructions of global temperature fields from reduced sets of representative locations in over-sampled regions (Jaume-Santero et al. 2020). The optimized reconstruction in the model experiment shows the same pattern of improvement (note the similarity between Fig. S7 and Fig. 4a), confirming that the reduction of biases in under-sampled regions is a robust feature of the optimized reconstruction, and relatively insensitive to the background state.

Interestingly, and despite the large differences in the distribution of weights for the observing networks of the early and late sub-periods (Fig. 3), they bring very similar patterns of improvement (Fig. 4). In particular, some of the largest increases in skill are observed over the southern half of the North Atlantic Ocean. Being far enough from major continental areas and the well sampled

European territories to yield skillful reconstructions, this region has often been disregarded in previous reconstructions (e.g., Küttel et al. 2010). However, regional SLP variations therein are of paramount importance for the climate of Europe and North and Central America by modulating the southern lobe of the NAO in winter and the intensity and location of the Azores-Bermuda Subtropical High in summer (Davis et al. 1997; Portis et al. 2001). The following sections focus on these seasonal aspects of the atmospheric circulation.

c. Climate variability and the Azores High

After demonstrating the added value of network weighting in the CRO-AM reconstructions, we analyze the SLP field reconstructed with the optimized weights for 1750-1835 and 1836-2004. The CRO-AM reconstruction yields more than 250 years of high-resolution monthly SLP fields over the North Atlantic, allowing us to study the major components of the North Atlantic atmospheric circulation that govern the climate conditions of its surroundings (i.e., Europe, Greenland, and the east coast of North America). Such is the case of the winter NAO (Hurrell and Deser 2010) and the East Atlantic (EA) pattern (Barnston and Livezey 1987; Mellado-Cano et al. 2019), the first and second leading modes of climate variability over the region. By using the CRO-AM reconstruction from 1750 to 2004, and the 20CRv3 reanalysis from 1836 to 2014, we derived the winter (DJF) indices of the NAO and EA for both datasets, defined as the first and second Principal Components (PC) of standardized SLP fields over [95°W - 50°E] and [20 - 73]°N. The amount of explained variance by the NAO and EA is 49.0% and 19.5% in the CRO-AM reconstruction, respectively, whereas the corresponding values for the NAO and EA in the 20CRv3 reanalysis are 38.7% and 17.2%. The same process was employed to generate the EA index from the seasonal SLP $5^\circ \times 5^\circ$ reconstruction of Küttel et al. (2010), which is provided for 1750-1886 and as an extension of the HadSLP2 (Allan and Ansell 2006). Deriving

a PC-based NAO index in Küttel et al. (2010) was hampered by its limited spatial coverage (the reconstruction stops at 40°W), and hence it was better obtained as the standardized SLP difference between Azores and Iceland, these regions being defined by the four closest grid points on the $5^\circ \times 5^\circ$ grid (Luterbacher et al. 2001). Our indices have also been compared against other NAO and EA instrumental-based indices from previous studies (Jones et al. 1997; Luterbacher et al. 2001; Comas-Bru and Hernández 2018), as defined in Table S1, obtaining statistically significant correlations ($p < 0.05$) with all of them, even before the twentieth century (Table 1).

Overall, the correlations are significantly higher for the NAO than for the EA index, arguably due to the degraded skill of the CRO-AM reconstruction over Europe further back in time. This would affect the node of the EA index in the monopole-based definitions, as well as the European node in the dipolar definitions of the EA. Note that, despite the diversity of data and methodologies employed for the construction of these indices, in all cases the CRO-AM NAO and EA indices yield higher correlations than their counterparts obtained from the reconstruction of (Küttel et al. 2010) that used wind records from ship logbooks over the ocean, in addition to many of the land-based observations. Although the comparison across indices must be taken with caution, and higher correlations do not necessarily involve more reliable reconstructions, results indicate that optimized networks of land-only observations might eventually outperform non-optimized networks including land and ocean records.

As the CRO-AM reconstruction brings the largest improvement over the AH region, we performed a more detailed assessment of the subtropical high for 1750-2004. In CRO-AM (Fig. 5a and b), the AH is readily identified from the seasonally averaged SLP fields of all winters and summers (JJA) of the 1751-2004 period. Spatial patterns of the AH show significant seasonal

differences, exhibiting a wider high pressure center across the Atlantic for summer, and a weaker system for winter as described in previous studies (Davis et al. 1997; Wanner et al. 1997; Portis et al. 2001; Küttel et al. 2010). The 1750-2004 evolution of the seasonal AH is depicted in Figs. 5c and d. Its intensity has been defined as the maximum $5^\circ \times 5^\circ$ mean SLP within the [20 – 55]°N and [10 – 70]°W domain. These criteria were chosen to facilitate the identification of the AH center and avoid misdetections, but the results are relatively robust to small changes in the selected domain. There are seasonal differences in the interannual evolution of the AH pressure system, with summers yielding quite stable values around 1024 hPa, and winters displaying larger variability on interannual and longer time scales, including a long-term increasing trend towards the end of the analyzed period.

To place this recent shift in the context of the last 250 years, we have computed trends of the winter AH intensity for running windows of 50 years from 1751 to 2004 CE (Fig. 6) with CRO-AM and compared them with those obtained, with the 20CRv3 reanalysis (1837-2013), and NCAR's SLP (1899-2019; Hurrell et al. (2020)). In all cases, winter decadal trends are small and show no large variations before 1900 CE, being followed by a sharp increase over 1953-2003, in agreement with Hasanean (2004). This change is concurrent with the prominent positive trend of the winter NAO from the 1960s to the 1990s (Pinto and Raible 2012, and references therein). Associated impacts of the recent AH strengthening have already been reported (e.g., Falarz 2019). The CRO-AM captures this trend and further reveals that it is unprecedented since 1750 CE, with the last 50 years exhibiting the largest intensification of the winter AH pressure system of the last two and half centuries (0.55 ± 0.19 hPa/10y). In contrast, an intensification of the AH pressure center is not observed during summer, although some studies using stream function as a diagnostic have reported a strengthening and westward movement of its western ridge over North America (Li

et al. 2012). The most striking feature of the long-term evolution of the summer AH is an overall intensification since the second half of the 18th century and during most of the 19th century (Figs. 5d and 6b). However, this trend coincides with the period of largest uncertainties, and hence the overall AH weakening towards the beginning of the analyzed period may result from limitations of the observing network (e.g., analogue fields poorly constrained by the scarcity of observations).

Furthermore, we have also assessed the contribution of AH pressure variations to the historical evolution of the NAO. To do so, the NAO index was decomposed as the standardized sum of its AH and IL components. They have been obtained separately as the projection of the winter CRO-AM anomalies onto the grid points where the NAO-related EOF pattern was strictly positive (AH) and negative (IL). Projections account for 55.4% of the total variance over the AH region and 49.7% over the IL region. Moreover, the sum of the AH and IL indices has a correlation of 0.99 and a RMSE of 0.11 with respect to the original NAO index for the 1751-2004 period. This linear behavior allows us to quantify the AH and IL contributions to the NAO value of each winter, and discern the dominant component through the analyzed period. The most influential action center is identified from the absolute values of the AH and IL indices. Figure 7a shows the time series of |AH| – |IL|, being this difference negative if the IL was predominant for a certain year and positive if the AH was the dominant one. Although AH and IL indices are strongly anti-correlated, there are few years with almost equal contributions to the NAO (e.g., |AH| – |IL| $\in$ (-0.1, 0.1) for 6.7% of winters during the 1751-2004 period). AH and IL dominant years tend to alternate throughout the period without a clear pattern. However, the time series displays some low-frequency variability as for instance the AH (IL) dominating the NAO over the second half of the 18th century (the first half of the 19th century), which, however, does not translate into systematic variations in the sign of the NAO index. Some of these periods are more evident at the beginning of the se-

ries, and may be affected by larger uncertainties of the CRO-AM reconstruction at that time (Fig. 5).

Figure 7a illustrates that differences in the reconstruction skill of the AH and IL would cause time-varying uncertainties with an impact on the magnitude and even the sign of the NAO (note that 45% of the winters have absolute |AH|-|IL| differences larger than 0.5 SD). To further address this issue, we have calculated the spread of the historical NAO values across the different indices defined in Table S1 and the PC-based NAO from the 20CRv3 reanalysis. The analysis has been restricted to 1900-2004, since the number of available indices decreases backwards. Interestingly, the evolution of the NAO spread from 1900 to 2004 tends to follow that of the |AH| - |IL| difference in AH dominant years (|AH| - |IL|>0), indicating that the more dominant the AH was with respect to the IL, the higher the differences between NAO series. Indeed, the Pearson correlation coefficient between the NAO spread and |AH| - |IL| series is 0.24, but increases to 0.36 ($p<0.01$) for AH dominant years. This is better illustrated in Fig. 7b where the analysis is separated for AH and IL dominant years. The results indicate that the NAO spread increases with the degree of AH dominance, this relationship being absent for IL years. Accordingly, NAO indices tend to show better agreement in years dominated by the IL and higher discrepancies for years when the NAO was largely determined by AH anomalies. Part of NAO disparities are expected to arise from differences in the NAO definition. However, we still find significant correlations in leave-one experiments that exclude one of the NAO indices from the analysis, without reporting systematic differences between PC- and station-based indices. As these NAO indices are obtained from station-based observations or instrumental SLP fields, the result points to different levels of performance in these datasets to capture the winter AH pressure system. This stresses the added value of the CRO-AM reconstruction, which brings a significant increase in the SLP skill over the AH region (Fig. 4), and of network optimization as a way to overcome potential shortcomings

affecting instrumental datasets. Uncertainties in the AH could in turn obscure the actual impact of this high pressure system on regional climates. Following previous studies that have found a higher influence of the IL (in comparison to the AH) on interannual climate fluctuations over different northern regions of the North Atlantic such as the Gulf Stream North Wall (e.g., Hameed and Piontkovski 2004; Sanchez-Franks et al. 2016), Germany (e.g., Riaz et al. 2017), and Greenland (Berdahl et al. 2018)), the CRO-AM reconstruction could be employed to better benchmark the regions and level of influence of the AH.

In summer, the AH increases its areal extent and intensity. Although interannual changes in intensity are relatively small (Fig. 5d), variations in location or extension can be pronounced and could affect the climate conditions of the surrounding continental regions in subtropical and mid-latitudes (Davis et al. 1997; Li et al. 2012). Thanks to the high resolution of CRO-AM, it has been possible to trace the AH center from 1750 to 2004 CE, defined as the central location of the $5^\circ \times 5^\circ$ box with maximum averaged SLP, among those within the [20 – 55]°N and [10 – 70]°W domain. The results indicate that the center of action has not experienced long-term changes in location, typically being situated within [34 – 39]°N and [26 – 39]°W. Despite the relatively stable locations of the summer AH center over the 250 years, we found some pronounced excursions. The largest one corresponds to an extreme shift towards the northeast (43°N and 18°W) in the summer of 1783 CE (Fig. 8). This year is remembered by the great dry fog in Europe (Stothers 1996; Thordarson and Self 2003; Schmidt et al. 2012) after the Laki eruption (Iceland) in June, and the significant cooling during the following winters (Luterbacher et al. 2004).

In contrast, reconstructed temperatures (Luterbacher et al. 2004) for that summer show an European-mean warming of ~3°C, being particularly pronounced in western Europe. Previous

studies have already acknowledged the difficulty of general circulation models to reproduce such warming event as a fast response to the volcanic forcing (Zambri et al. 2019), and have rather associated this extreme summer to persistent atmospheric blocking conditions, more likely caused by internal variability. Our results only partially support this hypothesis. While blocking events often cause extremely warm conditions in Europe (Barriopedro et al. 2011), they typically occur in northern latitudes of the continent and are rarely accompanied by anomalies in the summer AH such as those revealed by the CRO-AM reconstruction. The latter are more typically associated with meridional excursions of subtropical air masses towards western Europe, which can cause simultaneous extreme conditions over a large range of latitudes (e.g., the 2003 mega-heatwave, or the more recent 2019 European heatwave) (Sousa et al. 2018, 2019). Consistently, Fig. 8a shows how the AH pressure pattern obtained from CRO-AM was abnormally elongated towards the northeast during that summer, resulting on higher-than-normal SLP values over western Europe that are in good agreement with the warming inferred from independent temperature reconstructions. The meridional excursion of the summer AH is among the largest ones in our 250 year-long record, which could explain why extreme temperatures reached unusual poleward latitudes, exceeding the record-breaking values of the 2019 warm air intrusion reported so far (Sousa et al. 2019). Similar patterns are obtained when comparing composited SLP and temperature fields for summers with AH centers situated at the top ten northeasternmost vs top ten southwesternmost locations for the 1750-2002 period (Fig. S8), confirming the pronounced warming (especially in northern Europe) associated with northeast displacements of the AH. Future projections indicate an intensification, poleward shift and expansion of the summer AH pressure system, particularly towards the northwest and secondarily the northeast (He et al. 2017; Cherchi et al. 2018). Although significant trends in the latter are not detected yet, Figs. 8 and S8 may represent examples of European summers that are still to come.

5. Summary and conclusions

In this study we have shown that evolutionary algorithms can improve the performance of atmospheric circulation reconstructions over the North Atlantic-European area by optimizing the network of observations. By coupling an evolutionary algorithm known as the Coral Reef Optimization (CRO) with the Analogue Method (AM), we derive optimal sets of weights that maximize the skill of a network formed by 101 station-based observations of monthly SLP over the North Atlantic from 1750 to 2004 CE. The optimization process exploits the information of the predicting network, taking into account changes in data availability, as well as inconsistencies within the network. The robust relationships learned by the CRO algorithm are transformed in local weights during the AM reconstruction of the large-scale SLP field, improving the performance of reconstructions over almost the entire region (especially around the North Atlantic Ocean). Additional pseudo-reconstruction experiments using reanalysis and CMIP6 model data with the same constraints in data availability show that the spatial distribution of weights and the pattern of improvement are robust to the reference dataset and internal variations of the large-scale field targeted by the reconstruction. This is in agreement with the pseudo-reconstructions of Jaume-Santero et al. (2020), who also demonstrated that the CRO brings similar increases in performance for different reconstruction techniques.

The results show that changes in spatio-temporal data availability affect the representativeness of local observations in the network, arising as a key source of uncertainty in our SLP reconstructions. This result justified a separate optimization of the observing network for the earlier reconstruction period (1750-1835), which displayed marked changes in the number and coverage of observations as compared to the remaining period. A generalized improvement is reached at the expense

of sacrificing the reconstruction skill over the over-represented region of Europe, but this is compensated by comparatively larger improvements over the North Atlantic. This trade-off can be admissible for reconstructions of dynamical fields, which are mainly concerned with internal and forced aspects of the main modes of variability with major action centers located over the oceans.

The CRO-AM reconstruction provides high-resolution monthly SLP fields over the North Atlantic and Europe for 1750-2004. As the reconstruction is significantly improved over the ocean, we also derive new seasonal indices for the main modes of climate variability of the North Atlantic, such as the North Atlantic Oscillation (NAO), and its main action centers, namely, the Azores High (AH) and the Iceland Low (IL). They are obtained from a principal component (PC) analysis, and show an overall good agreement with series generated from independent station-based observations and spatially resolved fields, providing the longest instrumental PC-based NAO and EA indices. In particular, we have focused on the AH, as it covers the region with the largest improvement in the CRO-AM reconstruction compared to reconstructions generated with a non-optimized network of observations.

Our results show contrasts in the seasonal behavior of the AH pressure system, with larger interannual and long-term variations in intensity during winter, and relatively more stable conditions during summer. Despite the lack of long-term trends in the summer AH, the action center can experience substantial changes in location/extension that match with anomalous conditions inferred from independent temperature reconstructions and serve as historical analogues of future summers under the projected northern shift and expansion of the summer AH (Cherchi et al. 2018). On the contrary, our reconstructions capture changes in the winter AH during the second half of the 20th century until 2002 CE and reveal that this recent intensification has no

precedents in at least the last 250 years. The strengthening of the winter AH is timely with the well-reported positive NAO trend of 1960s-1990s (e.g., a positive winter AH trend around 1980 in agreement with Davis et al. 1997). While different causes have been proposed for this NAO trend, including anthropogenic factors, several studies show that it is not statistically distinguishable from atmosphere-ocean internal variability, or exceptional as compared to pre-industrial periods before 1650 CE (Pinto and Raible 2012, and references therein). This may be the case of the trend in the winter AH, whose changes in intensity have been associated with North Atlantic sea surface temperature anomalies (Falarz 2019). Our reconstruction provides a longer historical context of the AH pressure system and a more robust benchmark of pre-industrial conditions to explore the causes of this trend as well as sources of multi-decadal variability.

The recent intensification of the winter AH pressure system has not increased the influence of the winter AH on the NAO, which has been equally affected by anomalies in the AH and IL during the 1750-2004 period. However, the contribution of the AH and IL to the winter NAO index can substantially vary from one year to the next, with some winters being dominated by one or another action center. In spite of their similar levels of influence, our results show that the spread among NAO indices is larger for winters when the NAO was dominated by anomalies in the AH pressure system. As such, current discrepancies in instrumental NAO indices would stem more from uncertainties in the AH than in the IL. This points to limitations of current datasets to capture the historical evolution of the AH, and stresses the need for improved SLP reconstructions over this region. Our results highlight the potential value of meta-heuristic techniques such as the CRO algorithm in this avenue. These optimization methods make a step forward when compared to previous efforts, which have focused on sequential approaches (i.e. individual solutions based on subsets of best-performing records, Bradley (1996)). Although sequential methods perform well

for linear problems, genetic algorithms like the CRO are more efficient in finding good-enough solutions to non-linear problems such as those of the climate system (Salcedo-Sanz et al. 2019; Jaume-Santero et al. 2020). In addition, optimized weighting exploits the full network, avoiding the loss of information by the selection of best-performing subsets in sequential approaches. The CRO has also benefits in terms of computational needs, as it searches for possible solutions simultaneously, which makes the procedure highly parallelizable.

Acknowledgments. This work was supported by the Ministerio de Economía y Competitividad del Gobierno de España through the PALEOSTRAT (CGL2015-69699-R) project, and by the European Commission through the H2020 EU CLINT project (Grant Agreement No. 101003876). Jaume-Santero was funded by grant BES-2016-077030 from the Ministerio de Ciencia e Innovación and the Ministerio de Universidades of the Spanish government.

Data availability statement. The datasets generated in this paper are publicly available at https://doi.org/10.6084/m9.figshare.13633898.v1

References

Allan, R., and T. Ansell, 2006: A New Globally Complete Monthly Historical Gridded Mean Sea Level Pressure Dataset (HadSLP2): 1850-2004. *J. Clim.*, **19 (22)**, 5816–5842, doi:10.1175/JCLI3937.1, URL https://doi.org/10.1175/JCLI3937.1, https://journals.ametsoc.org/jcli/article-pdf/19/22/5816/3799923/jcli3937_1.pdf.

Barnes, E. A., J. W. Hurrell, I. Ebert-Uphoff, C. Anderson, and D. Anderson, 2019: Viewing Forced Climate Patterns Through an AI Lens. *Geophys. Res. Lett.*, **46 (22)**, 13 389–13 398, doi:10.1029/2019GL084944, URL https://doi.org/10.1029/2019GL084944.

Barnston, A. G., and R. E. Livezey, 1987: Classification, Seasonality and Persistence of Low-Frequency Atmospheric Circulation Patterns. *Mon. Weather Rev.*, **115 (6)**, 1083–1126, doi:10.1175/1520-0493(1987)115<1083:CSAPOL>2.0.CO;2, URL https://journals.ametsoc.org/view/journals/mwre/115/6/1520-0493_1987_115_1083_csapol_2_0_co_2.xml.

Barriopedro, D., E. M. Fischer, J. Luterbacher, R. M. Trigo, and R. García-Herrera, 2011: The Hot Summer of 2010: Redrawing the Temperature Record Map of Europe. *Science*, **332 (6026)**, 220, doi:10.1126/science.1201224, URL http://science.sciencemag.org/content/332/6026/220.abstract.

Berdahl, M., and Coauthors, 2018: Southeast Greenland winter precipitation strongly linked to the Icelandic low position. *J. Clim.*, **31 (11)**, 4483–4500, doi:10.1175/JCLI-D-17-0622.1, URL https://doi.org/10.1175/JCLI-D-17-0622.1.

Bladé, I., D. Fortuny, G. J. van Oldenborgh, and B. Liebmann, 2012: The summer North Atlantic Oscillation in CMIP3 models and related uncertainties in projected summer drying in Europe. *J. Geophys. Res. Atmos.*, **117 (D16)**, doi:10.1029/2012JD017816, URL https://doi.org/10.1029/2012JD017816.

Bothe, O., and E. Zorita, 2020: Proxy surrogate reconstructions for Europe and the estimation of their uncertainties. *Clim. Past*, **16 (1)**, 341–369, doi:10.5194/cp-16-341-2020, URL https://cp.copernicus.org/articles/16/341/2020/.

Bradley, R. S., 1996: Are there optimum sites for global paleotemperature reconstruction? *(eds. Jones P.D., Bradley R.S., Jouzel J.) Climatic variations and forcing mechanisms of the last 2000 years. NATO ASI Series (Series I: Global Environmental Change)*, 603–624.

Brönnimann, S., and Coauthors, 2020: Unlocking Pre-1850 Instrumental Meteorological Records: A Global Inventory. *BAMS*, **100 (12)**, ES389–ES413, doi:10.1175/BAMS-D-19-0040.1, URL https://doi.org/10.1175/BAMS-D-19-0040.1, https://journals.ametsoc.org/bams/article-pdf/100/12/ES389/4951704/bams-d-19-0040_1.pdf.

Carro-Calvo, L., F. Jaume-Santero, R. García-Herrera, and S. Salcedo-Sanz, 2020: k-Gaps: a novel technique for clustering incomplete climatological time series. *Theor. Appl. Climatol.*, doi:10.1007/s00704-020-03396-w, URL https://doi.org/10.1007/s00704-020-03396-w.

Casty, C., C. C. Raible, T. F. Stocker, H. Wanner, and J. Luterbacher, 2007: A European pattern climatology 1766–2000, journal=Clim. Dyn. **29 (7)**, 791–805, doi:10.1007/s00382-007-0257-6, URL https://doi.org/10.1007/s00382-007-0257-6.

Cherchi, A., T. Ambrizzi, S. Behera, A. C. V. Freitas, Y. Morioka, and T. Zhou, 2018: The Response of Subtropical Highs to Climate Change. *Curr. Clim.*, **4 (4)**, 371–382, doi:10.1007/s40641-018-0114-1, URL https://doi.org/10.1007/s40641-018-0114-1.

Christensen, J. H., and Coauthors, 2013: Climate Phenomena and their Relevance for Future Regional Climate Change. *Climate Change 2013: The Physical Science Basis. Contribution of Working Group I to the Fifth Assessment Report of the Intergovernmental Panel on Climate Change*, T. F. Stocker, D. Qin, G.-K. Plattner, M. Tignor, S. K. Allen, J. Doschung, A. Nauels, Y. Xia, V. Bex, and P. M. Midgley, Eds., Cambridge University Press, Cambridge, United Kingdom and New York, NY, USA, 1217–1308.

Comas-Bru, L., and A. Hernández, 2018: Reconciling north atlantic climate modes: revised monthly indices for the east atlantic and the scandinavian patterns beyond the 20th century. *Earth Syst. Sci. Data*, **10 (4)**, 2329–2344, doi:10.5194/essd-10-2329-2018, URL https://essd.copernicus.org/articles/10/2329/2018/.

Cook, E. R., Y. Kushnir, J. E. Smerdon, A. P. Williams, K. J. Anchukaitis, and E. R. Wahl, 2019: A Euro-Mediterranean tree-ring reconstruction of the winter NAO index since 910 C.E. *Clim. Dyn.*, **53 (3)**, 1567–1580, doi:10.1007/s00382-019-04696-2, URL https://doi.org/10.1007/s00382-019-04696-2.

Cram, T. A., and Coauthors, 2015: The International Surface Pressure Databank version 2. *Geosci. Data J.*, **2 (1)**, 31–46, doi:10.1002/gdj3.25, URL https://doi.org/10.1002/gdj3.25.

Davis, R. E., B. P. Hayden, D. A. Gay, W. L. Phillips, and G. V. Jones, 1997: The North Atlantic Subtropical Anticyclone. *J. Clim.*, **10 (4)**, 728–744, doi:10.1175/1520-0442(1997)010<0728:TNASA>2.0.CO;2, URL https://journals.ametsoc.org/view/journals/clim/10/4/1520-0442_1997_010_0728_tnasa_2.0.co_2.xml.

Eiben, A. E., and J. Smith, 2015: From evolutionary computation to the evolution of things. *Nature*, **521**, doi:10.1038/nature14544, URL https://doi.org/10.1038/nature14544.

Eyring, V., S. Bony, G. A. Meehl, C. A. Senior, B. Stevens, R. J. Stouffer, and K. E. Taylor, 2016: Overview of the Coupled Model Intercomparison Project Phase 6 (CMIP6) experimental design and organization. *Geosci. Model Dev.*, **9 (5)**, 1937–1958, doi:10.5194/gmd-9-1937-2016, URL https://gmd.copernicus.org/articles/9/1937/2016/.

Falarz, M., 2019: Azores High and Hawaiian High: correlations, trends and shifts (1948–2018). *Theor. Appl. Climatol.*, **138 (1-2)**, 417–431, doi:10.1007/s00704-019-02837-5, URL https://doi.org/10.1007/s00704-019-02837-5.

Folland, C. K., J. Knight, H. W. Linderholm, D. Fereday, S. Ineson, and J. W. Hurrell, 2009: The Summer North Atlantic Oscillation: Past, Present, and Future. *J. Clim.*, **22 (5)**, 1082–

1103, doi:10.1175/2008JCLI2459.1, URL https://journals.ametsoc.org/view/journals/clim/22/5/2008jcli2459.1.xml.

Forrest, S., 1993: Genetic algorithms: principles of natural selection applied to computation. *Science*, **261**, doi:10.1126/science.8346439, URL https://doi.org/10.1126/science.8346439.

Franke, J., S. Brönnimann, J. Bhend, and Y. Brugnara, 2017: A monthly global paleo-reanalysis of the atmosphere from 1600 to 2005 for studying past climatic variations. *Sci. Data*, **4**, doi:10.1038/sdata.2017.76, URL https://doi.org/10.1038/sdata.2017.76.

Franke, J., J. F. González-Rouco, D. Frank, and N. E. Graham, 2011: 200 years of European temperature variability: insights from and tests of the proxy surrogate reconstruction analog method. *Clim. Dyn.*, **37 (1)**, 133–150, doi:10.1007/s00382-010-0802-6, URL https://doi.org/10.1007/s00382-010-0802-6.

Freeman, E., and Coauthors, 2017: ICOADS Release 3.0: a major update to the historical marine climate record. *Int. J. Climatol.*, **37 (5)**, 2211–2232, doi:10.1002/joc.4775, URL https://doi.org/10.1002/joc.4775.

García-Herrera, R., D. Barriopedro, D. Gallego, J. Mellado-Cano, D. Wheeler, and C. Wilkinson, 2018: Understanding weather and climate of the last 300 years from ships' logbooks. *WIREs Clim. Change*, **9 (6)**, e544, doi:10.1002/wcc.544, URL https://doi.org/10.1002/wcc.544.

Gómez-Navarro, J. J., J. Werner, S. Wagner, J. Luterbacher, and E. Zorita, 2015: Establishing the skill of climate field reconstruction techniques for precipitation with pseudoproxy experiments. *Clim. Dyn.*, **45 (5)**, 1395–1413, doi:10.1007/s00382-014-2388-x, URL https://doi.org/10.1007/s00382-014-2388-x.

Gómez-Navarro, J. J., E. Zorita, C. C. Raible, and R. Neukom, 2017: Pseudo-proxy tests of the analogue method to reconstruct spatially resolved global temperature during the Common Era. *Clim. Past*, **13**, doi:10.5194/cp-13-629-2017, URL https://doi.org/10.5194/cp-13-629-2017.

Graham, N. E., C. M. Ammann, D. Fleitmann, K. M. Cobb, and J. Luterbacher, 2011: Support for global climate reorganization during the "Medieval Climate Anomaly". *Clim. Dyn.*, **37 (5)**, 1217–1245, doi:10.1007/s00382-010-0914-z, URL https://doi.org/10.1007/s00382-010-0914-z.

Hameed, S., and S. Piontkovski, 2004: The dominant influence of the Icelandic Low on the position of the Gulf Stream northwall. *Geophys. Res. Lett.*, **31 (9)**, doi:10.1029/2004GL019561, URL https://doi.org/10.1029/2004GL019561.

Hasanean, H. M., 2004: Variability of the North Atlantic subtropical high and associations with tropical sea-surface temperature. *Int. J. Climatol.*, **24 (8)**, 945–957, doi:10.1002/joc.1042, URL https://doi.org/10.1002/joc.1042.

He, C., B. Wu, L. Zou, and T. Zhou, 2017: Responses of the Summertime Subtropical Anticyclones to Global Warming. *J. Clim.*, **30 (16)**, 6465–6479, doi:10.1175/JCLI-D-16-0529.1, URL https://journals.ametsoc.org/view/journals/clim/30/16/jcli-d-16-0529.1.xml.

Hernández, A., and Coauthors, 2020: A 2000-year Bayesian NAO reconstruction from the Iberian Peninsula. *Sci. Rep.*, **10 (1)**, 14 961, doi:10.1038/s41598-020-71372-5, URL https://doi.org/10.1038/s41598-020-71372-5.

Hordon, R. M., 1987: *Icelandic low*, 514–515. Springer US, Boston, MA, doi:10.1007/0-387-30749-4_92, URL https://doi.org/10.1007/0-387-30749-4_92.

Hurrell, J., K. Trenberth, and NCAR, 2020: The Climate Data Guide: NCAR Sea Level Pressure. *(Eds. National Center for Atmospheric Research Staff) Retrieved*

from https://climatedataguide.ucar.edu/climate-data/ncar-sea-level-pressure, URL https://climatedataguide.ucar.edu/climate-data/ncar-sea-level-pressure.

Hurrell, J. W., 1995: Decadal Trends in the North Atlantic Oscillation: Regional Temperatures and Precipitation. *Science*, **269 (5224)**, 676, doi:10.1126/science.269.5224.676, URL http://science.sciencemag.org/content/269/5224/676.abstract.

Hurrell, J. W., and C. Deser, 2010: North Atlantic climate variability: The role of the North Atlantic Oscillation. *J. Mar. Syst.*, **78 (1)**, 28 – 41, doi:10.1016/j.jmarsys.2008.11.026, URL http://www.sciencedirect.com/science/article/pii/S0924796309000815.

Iqbal, M. J., S. U. Rehman, S. Hameed, and M. A. Qureshi, 2019: Changes in Hadley circulation: the Azores high and winter precipitation over tropical northeast Africa. *Theor. Appl. Climatol.*, **137 (3-4)**, 2941–2948, doi:10.1007/s00704-019-02765-4, URL https://link.springer.com/article/10.1007/s00704-019-02765-4.

Jaume-Santero, F., D. Barriopedro, R. García-Herrera, N. Calvo, and S. Salcedo-Sanz, 2020: Selection of optimal proxy locations for temperature field reconstructions using evolutionary algorithms. *Sci. Rep.*, **10 (1)**, doi:10.1038/s41598-020-64459-6, URL https://doi.org/10.1038/s41598-020-64459-6.

Jones, P. D., T. Jonsson, and D. Wheeler, 1997: Extension to the North Atlantic oscillation using early instrumental pressure observations from Gibraltar and south-west Iceland. *Int. J. Clim.*, **17 (13)**, 1433–1450, doi:10.1002/(SICI)1097-0088(19971115)17:13<1433::AID-JOC203>3.0.CO;2-P, URL https://doi.org/10.1002/(SICI)1097-0088(19971115)17:13<1433::AID-JOC203>3.0.CO;2-P.

Jungclaus, J. H., and Coauthors, 2017: The PMIP4 contribution to CMIP6 – Part 3: The last millennium, scientific objective, and experimental design for the PMIP4 *past1000*simulations. *Geosci. Model Dev.*, **10 (11)**, 4005–4033, doi:10.5194/gmd-10-4005-2017, URL https://gmd.copernicus.org/articles/10/4005/2017/.

Kadow, C., D. M. Hall, and U. Ulbrich, 2020: Artificial intelligence reconstructs missing climate information. *Nat. Geosci.*, **13 (6)**, 408–413, doi:10.1038/s41561-020-0582-5, URL https://doi.org/10.1038/s41561-020-0582-5.

Küttel, M., and Coauthors, 2010: The importance of ship log data: reconstructing North Atlantic, European and Mediterranean sea level pressure fields back to 1750. *Clim. Dyn.*, **34 (7)**, 1115–1128, doi:10.1007/s00382-009-0577-9, URL https://doi.org/10.1007/s00382-009-0577-9.

LeCun, Y., Y. Bengio, and G. Hinton, 2015: Deep Learning. *Nature*, **521 (7553)**, 436–444, doi:10.1038/nature14539, URL https://doi.org/10.1038/nature14539.

Li, W., L. Li, M. Ting, and Y. Liu, 2012: Intensification of Northern Hemisphere subtropical highs in a warming climate. *Nat. Geosci.*, **5 (11)**, 830–834, doi:10.1038/ngeo1590, URL https://doi.org/10.1038/ngeo1590.

Lorenz, E. N., 1969: Atmospheric Predictability as Revealed by Naturally Occurring Analogues. *J. Atmos. Sci.*, **26 (4)**, 636–646, doi:10.1175/1520-0469(1969)26<636:APARBN>2.0.CO;2, URL https://journals.ametsoc.org/view/journals/atsc/26/4/1520-0469_1969_26_636_aparbn_2_0_co_2.xml.

Luterbacher, J., D. Dietrich, E. Xoplaki, M. Grosjean, and H. Wanner, 2004: European Seasonal and Annual Temperature Variability, Trends, and Extremes Since 1500. *Science*, **303 (5663)**,

1499–1503, doi:10.1126/science.1093877, URL https://science.sciencemag.org/content/303/5663/1499, https://science.sciencemag.org/content/303/5663/1499.full.pdf.

Luterbacher, J., C. Schmutz, D. Gyalistras, E. Xoplaki, and H. Wanner, 1999: Reconstruction of monthly NAO and EU indices back to AD 1675. *Geophys. Res. Lett.*, **26 (17)**, 2745–2748, doi:10.1029/1999GL900576, URL https://doi.org/10.1029/1999GL900576.

Luterbacher, J., and Coauthors, 2001: Extending North Atlantic oscillation reconstructions back to 1500. *Atmos. Sci. Lett*, **2 (1-4)**, 114–124, doi:10.1006/asle.2002.0047, URL https://rmets.onlinelibrary.wiley.com/doi/abs/10.1006/asle.2002.0047, https://rmets.onlinelibrary.wiley.com/doi/pdf/10.1006/asle.2002.0047.

Luterbacher, J., and Coauthors, 2002: Reconstruction of sea level pressure fields over the Eastern North Atlantic and Europe back to 1500. *Clim. Dyn.*, **18 (7)**, 545–561, doi:10.1007/s00382-001-0196-6, URL https://doi.org/10.1007/s00382-001-0196-6.

Mellado-Cano, J., D. Barriopedro, R. García-Herrera, R. M. Trigo, and A. Hernández, 2019: Examining the North Atlantic Oscillation, East Atlantic Pattern, and Jet Variability since 1685. *J. Clim.*, **32 (19)**, 6285–6298, doi:10.1175/JCLI-D-19-0135.1, URL https://doi.org/10.1175/JCLI-D-19-0135.1, https://journals.ametsoc.org/jcli/article-pdf/32/19/6285/4840987/jcli-d-19-0135_1.pdf.

Noone, S., and Coauthors, 2020: Progress towards a holistic land and marine surface meteorological database and a call for additional contributions. *Geosci. Data J.*, doi:10.1002/gdj3.109, URL https://doi.org/10.1002/gdj3.109.

Ortega, P., F. Lehner, D. Swingedouw, V. Masson-Delmotte, C. C. Raible, M. Casado, and P. Yiou, 2015: A model-tested North Atlantic Oscillation reconstruction for the past millennium. *Nature*,

523 (7558), 71–74, doi:10.1038/nature14518, URL https://doi.org/10.1038/nature14518.

Pinto, J. G., and C. C. Raible, 2012: Past and recent changes in the North Atlantic oscillation. *WIREs Clim. Change*, **3 (1)**, 79–90, doi:10.1002/wcc.150, URL https://doi.org/10.1002/wcc.150.

Portis, D. H., J. E. Walsh, M. El Hamly, and P. J. Lamb, 2001: Seasonality of the North Atlantic Oscillation. *J. Clim.*, **14 (9)**, 2069–2078, doi:10.1175/1520-0442(2001)014<2069:SOTNAO>2.0.CO;2, URL https://journals.ametsoc.org/view/journals/clim/14/9/1520-0442_2001_014_2069_sotnao_2.0.co_2.xml.

Riaz, S. M. F., M. J. Iqbal, and S. Hameed, 2017: Impact of the North Atlantic Oscillation on winter climate of Germany. *Tellus A: Dyn. Meteorol. Oceanogr.*, **69 (1)**, 1406 263, doi:10.1080/16000870.2017.1406263, URL https://doi.org/10.1080/16000870.2017.1406263.

Sahsamanoglou, H. S., 1990: A contribution to the study of action centres in the North Atlantic. *Int. J. Climatol.*, **10 (3)**, 247–261, doi:10.1002/joc.3370100303, URL https://doi.org/10.1002/joc.3370100303.

Salcedo-Sanz, S., 2017: A review on the coral reefs optimization algorithm: new development lines and current applications. *Prog. Artif. Intell.*, **6**, doi:10.1007/s13748-016-0104-2, URL https://doi.org/10.1007/s13748-016-0104-2.

Salcedo-Sanz, S., R. García-Herrera, C. Camacho-Gómez, E. Alexandre, L. Carro-Calvo, and F. Jaume-Santero, 2019: Near-optimal selection of representative measuring points for robust temperature field reconstruction with the CRO-SL and analogue methods. *Glob. Planet. Change*, **178**, 15–34, doi:10.1016/j.gloplacha.2019.04.013, URL https://doi.org/10.1016/j.gloplacha.2019.04.013.

Salcedo-Sanz, S., R. García-Herrera, C. Camacho-Gómez, A. Aybar-Ruíz, and E. Alexandre, 2018: Wind power field reconstruction from a reduced set of representative measuring points. *Appl. Energ.*, **228**, doi:10.1016/j.apenergy.2018.07.003, URL https://doi.org/10.1016/j.apenergy.2018.07.003.

Sanchez-Franks, A., S. Hameed, and R. E. Wilson, 2016: The Icelandic low as a predictor of the Gulf Stream north wall position. *J. Phys. Oceanogr.*, **46 (3)**, 817–826, doi:10.1175/JPO-D-14-0244.1, URL https://doi.org/10.1175/JPO-D-14-0244.1.

Schmidt, A., T. Thordarson, L. D. Oman, A. Robock, and S. Self, 2012: Climatic impact of the long-lasting 1783 Laki eruption: Inapplicability of mass-independent sulfur isotopic composition measurements. *J. Geophys. Res. Atmos.*, **117 (D23)**, doi:10.1029/2012JD018414, URL https://doi.org/10.1029/2012JD018414.

Schmutz, C., J. Luterbacher, D. Gyalistras, E. Xoplaki, and H. Wanner, 2000: Can we trust proxy-based NAO index reconstructions? *Geophys. Res. Lett.*, **27 (8)**, 1135–1138, doi:10.1029/1999GL011045, URL https://doi.org/10.1029/1999GL011045.

Slivinski, L. C., and Coauthors, 2019: Towards a more reliable historical reanalysis: Improvements for version 3 of the Twentieth Century Reanalysis system. *Q. J. R. Meteorol. Soc.*, **145 (724)**, 2876–2908, doi:10.1002/qj.3598, URL https://rmets.onlinelibrary.wiley.com/doi/abs/10.1002/qj.3598, https://rmets.onlinelibrary.wiley.com/doi/pdf/10.1002/qj.3598.

Smerdon, J. E., 2011: Climate models as a test bed for climate reconstruction methods: pseudoproxy experiments. *WIREs: Clim. Change*, **3**, doi:10.1002/wcc.149, URL https://doi.org/10.1002/wcc.149.

Soto, R., J. A. Gómez-Pulido, S. Caro, and J. M. Lanza-Gutiérrez, 2019: Data Science and AI-Based Optimization in Scientific Programming. *Sci. Program.*, **2019**, 7154 765, doi:10.1155/2019/7154765, URL https://doi.org/10.1155/2019/7154765.

Sousa, P. M., D. Barriopedro, A. M. Ramos, R. García-Herrera, F. Espírito-Santo, and R. M. Trigo, 2019: Saharan air intrusions as a relevant mechanism for Iberian heatwaves: The record breaking events of August 2018 and June 2019. *Weather. Clim. Extremes*, **26**, 100 224, doi:10.1016/j.wace.2019.100224, URL http://www.sciencedirect.com/science/article/pii/S2212094719300349.

Sousa, P. M., R. M. Trigo, D. Barriopedro, P. M. M. Soares, and J. A. Santos, 2018: European temperature responses to blocking and ridge regional patterns. *Clim. Dyn.*, **50 (1)**, 457–477, doi:10.1007/s00382-017-3620-2, URL https://doi.org/10.1007/s00382-017-3620-2.

Srivastava, P. K., D. Han, M. A. Rico-Ramirez, M. Bray, and T. Islam, 2012: Selection of classification techniques for land use/land cover change investigation. *Adv. Space Res.*, **50 (9)**, 1250 – 1265, doi:10.1016/j.asr.2012.06.032, URL http://www.sciencedirect.com/science/article/pii/S0273117712004218.

Stothers, R. B., 1996: The Great Dry Fog of 1783. *Clim. Change*, **32**, 79–89, doi:10.1007/BF00141279.

Swarnkar, A., and A. Swarnkar, 2019: Artificial Intelligence Based Optimization Techniques: A Review. *(eds. Kalam A., Niazi K., Soni A., Siddiqui S., Mundra A.) Intelligent Computing Techniques for Smart Energy Systems. Lecture Notes in Electrical Engineering*.

Talento, S., L. Schneider, J. Werner, and J. Luterbacher, 2019: Millennium-length precipitation reconstruction over south-eastern Asia: a pseudo-proxy approach. *Earth Sys. Dyn.*, **10 (2)**, 347–364, doi:10.5194/esd-10-347-2019, URL https://esd.copernicus.org/articles/10/347/2019/.

Thordarson, T., and S. Self, 2003: Atmospheric and environmental effects of the 1783–1784 Laki eruption: A review and reassessment. *J. Geophys.Res. Atmos.*, **108 (D1)**, AAC 7–1–AAC 7–29, doi:10.1029/2001JD002042, URL https://doi.org/10.1029/2001JD002042.

Trigo, R. M., D. Pozo-Vázquez, T. J. Osborn, Y. Castro-Díez, S. Gámiz-Fortis, and M. J. Esteban-Parra, 2004: North Atlantic oscillation influence on precipitation, river flow and water resources in the Iberian Peninsula. *Int. J. Climatol.*, **24 (8)**, 925–944, doi:10.1002/joc.1048, URL https://doi.org/10.1002/joc.1048.

Vaccaro, A., J. Emile-Geay, D. Guillot, R. Verna, C. Morice, J. Kennedy, and B. Rajaratnam, 2021: Climate field completion via Markov random fields – Application to the HadCRUT4.6 temperature dataset. *J. Clim.*, 1–66, doi:10.1175/JCLI-D-19-0814.1, URL https://journals.ametsoc.org/view/journals/clim/aop/JCLI-D-19-0814.1/JCLI-D-19-0814.1.xml.

Vinther, B. M., K. K. Andersen, A. W. Hansen, T. Schmith, and P. D. Jones, 2003: Improving the Gibraltar/Reykjavik NAO index. *Geophys. Res. Lett.*, **30 (23)**, doi:10.1029/2003GL018220, URL https://doi.org/10.1029/2003GL018220.

Vrugt, J. A., and B. A. Robinson, 2007: Improved evolutionary optimization from genetically adaptive multimethod search. *PNAS*, **104**, doi:10.1073/pnas.0610471104, URL https://doi.org/10.1073/pnas.0610471104.

Wanner, H., R. Rickli, E. Salvisberg, C. Schmutz, and M. Schüepp, 1997: Global climate change and variability and its influence on Alpine climate — concepts and observations. *Theor. Appl. Climatol.*, **58 (3)**, 221–243, doi:10.1007/BF00865022, URL https://doi.org/10.1007/BF00865022.

Yukimoto, S., and Coauthors, 2019: The Meteorological Research Institute Earth System Model Version 2.0, MRI-ESM2.0: Description and Basic Evaluation of the Physical Component. *J.*

965 *Meteorol. Soc. Jpn. Ser. II*, **97 (5)**, 931–965, doi:10.2151/jmsj.2019-051.

966 Zambri, B., A. Robock, M. J. Mills, and A. Schmidt, 2019: Modeling the 1783-1784 Laki Eruption
967 in Iceland: 2. Climate Impacts. *J. Geophys. Res. Atmos.*, **124 (13)**, 6770–6790, doi:10.1029/
968 2018JD029554, URL https://agupubs.onlinelibrary.wiley.com/doi/abs/10.1029/2018JD029554,
969 https://agupubs.onlinelibrary.wiley.com/doi/pdf/10.1029/2018JD029554.

970 Zishka, K. M., and P. J. Smith, 1980: The Climatology of Cyclones and Anticyclones over
971 North America and Surrounding Ocean Environs for January and July, 1950–77. *Mon.*
972 *Weather Rev.*, **108 (4)**, 387–401, doi:10.1175/1520-0493(1980)108<0387:TCOCAA>2.0.CO;
973 2, URL https://journals.ametsoc.org/view/journals/mwre/108/4/1520-0493_1980_108_0387_
974 tcocaa_2_0_co_2.xml.

LIST OF TABLES

981 TABLE 1. Pearson correlation coefficients of winter NAO and EA indices. Correlations have been calculated
982 for the overlapping interval of each pair of indices within the 1751-1886 period (to avoid parts in some of the
983 series that were filled or extended with observations from other datasets). Coefficients in bold are statistically
984 significant at 95% confidence level.

	Period (CE)	CRO-AM	Küttel et al. (2010)
	NAO		
Jones et al. (1997)	1825 - 1886	**0.92**	**0.77**
Luterbacher et al. (2001)	1751 - 1886	**0.75**	**0.60**
Vinther et al. (2003)	1823 - 1886	**0.90**	**0.70**
	EA		
Comas-Bru and Hernández (2018)	1852-1886	**0.73**	0.28

LIST OF FIGURES

show winters with a leading influence of the Azores High and Iceland Low, respectively. The red line represents the spread (standard deviation) of NAO values for each winter of the 1900-2004 period, calculated from a suite of instrumental-based NAO (Table S1). (b) Scatter plot (1900-2004) of the spread of NAO indices for winters dominated by the Iceland Low (blue section) and the Azores High (orange section). Dashed lines represent separate linear regressions for each dominant component. Grey shading shows the 95% confidence interval of the linear fits. All series have been standardized with respect to the 1951-2000 baseline. 55

Fig. 8. Azores High shift in the extremely warm summer of 1783 CE. (a) Summer mean SLP (shading, in hPa) for 1783 obtained from the optimized reconstruction. (b) Summer mean temperature anomalies (in °C, with respect to 1500-2002) for 1783 as reconstructed by Luterbacher et al. (2004). Black diamonds with error bars show the climatological (1750-2002) location (mean and two standard deviations) of the Azores High center. Green crosses represent the center of the Azores High for the summer of 1783. 56

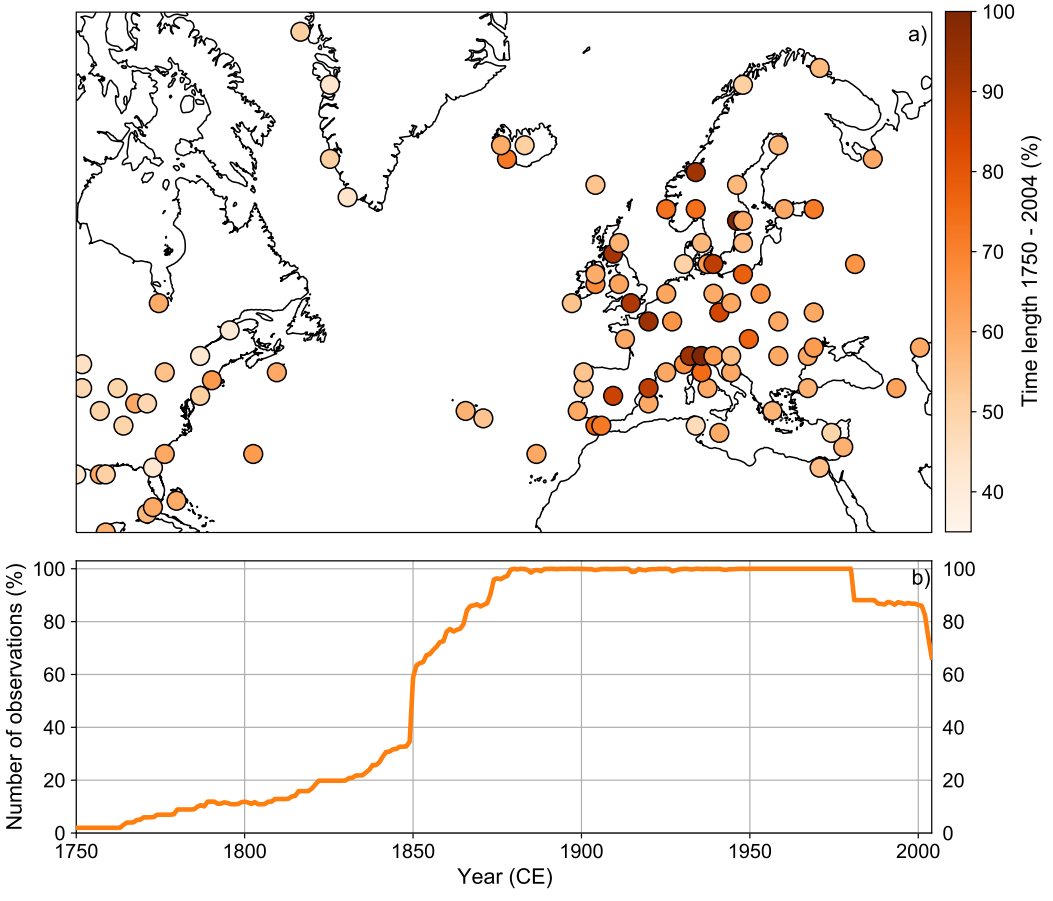

FIG. 1. Spatio-temporal distribution of SLP observations. (a) Spatial distribution of stations with monthly SLP observations for 1750-2004. Shading shows the percentage of time with available observations over the 1750-2004 period, with darker shading indicating longer time series. (b) Evolution of the frequency of observations (in percentage with respect to the total number of stations) for 1750-2004.

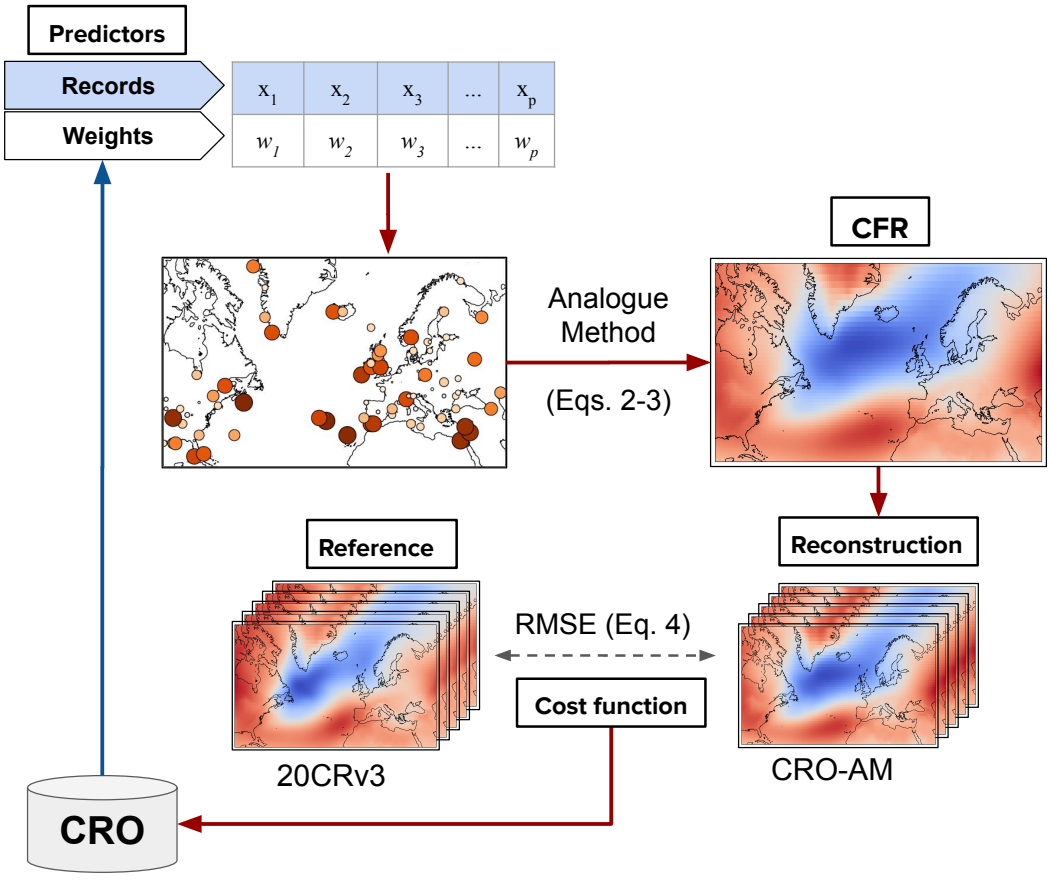

FIG. 2. Schematics of the optimized CRO-AM reconstruction depicting the reconstruction and optimization process. A set of weights (w_i, colored dots) are applied over the predicting network x_j of SLP observations available at each month for the reconstruction (infilling) of the monthly SLP field over the North Atlantic with the Analogue Method. The reconstruction error (RMSE) of the North Atlantic SLP field is subsequently assessed with respect to the reference target (20CRv3 reanalysis) over the reconstructed period. This metric is used by the CRO as a cost function during the optimization process, which proceeds iteratively applying search operators to the weights imposed in the reconstruction step in order to find an optimal set of weights that minimizes the RMSE.

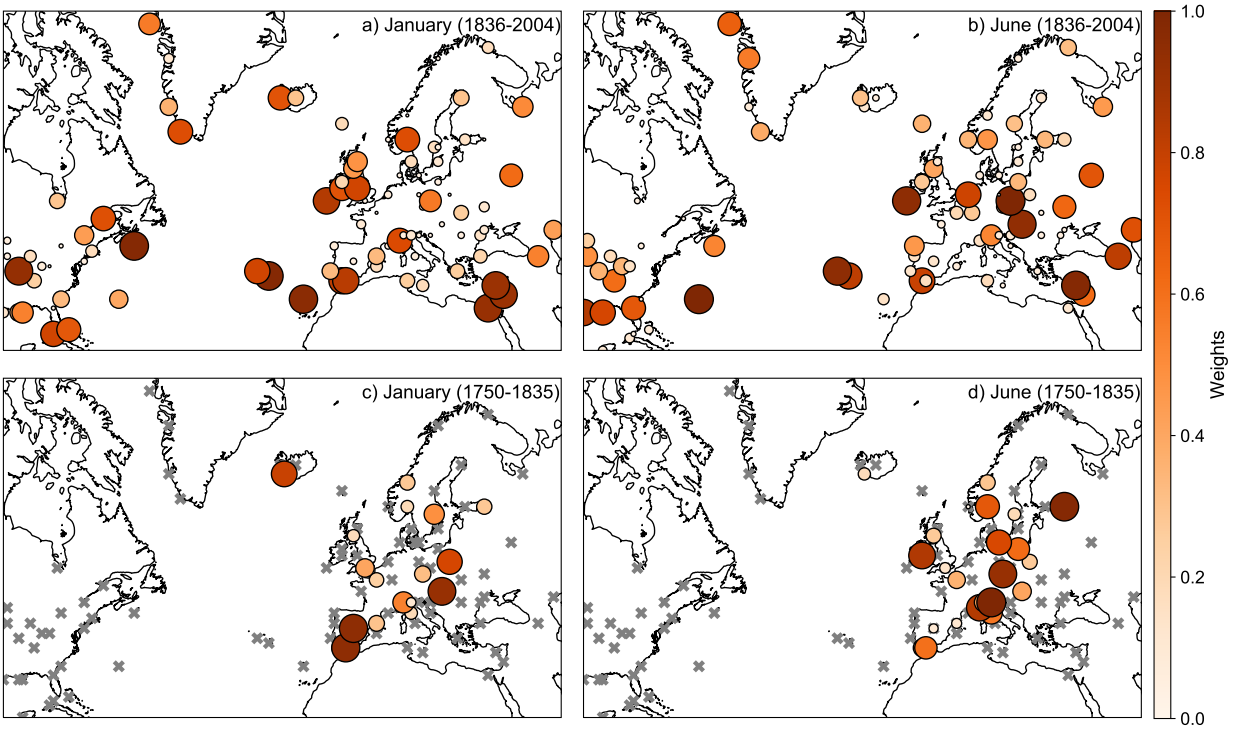

1057 FIG. 3. Spatial distribution of optimized monthly weights for the observing network obtained with the CRO-
1058 AM algorithm. Weights (from 0 to 1) apply to the observing network of (a, c) all Januaries, and (b,d) all Junes
1059 of the (a,c) 1750-1835 and (b,d) 1836-2004 period. The size of the dot is proportional to the magnitude of local
1060 weight, which is also indicated by shading. Grey crosses in (c) and (d) represent observations without available
1061 information for 1750-1835.

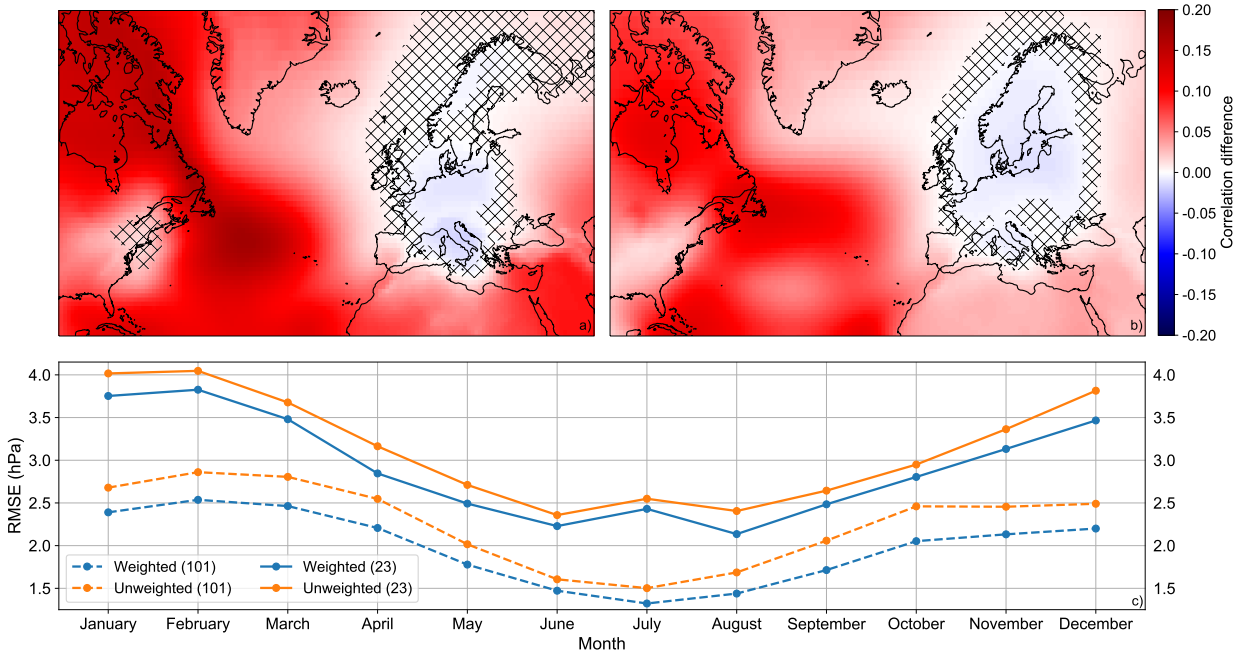

FIG. 4. Comparison of the SLP reconstruction skill obtained with and without optimization. (Top panels) Difference of performance (Pearson correlation coefficient with the 20CRv3 reanalysis) between the CRO-AM and AM SLP reconstructions generated with the observing network of: (a) 1750-1835; (b) 1836-2004. Crossed regions show non-significant differences ($p>0.05$). (c) Monthly mean evolution of the area-weighted root-mean-square error of the North Atlantic SLP (with respect to 20CRv3) for the CRO-AM (blue) and AM (orange) reconstruction and the observing network of 1750-1835 (solid) and 1836-2004 (dashed). The performance of the 1750-1835 network is evaluated over the 1919-2004 period of the reanalysis. See text for details.

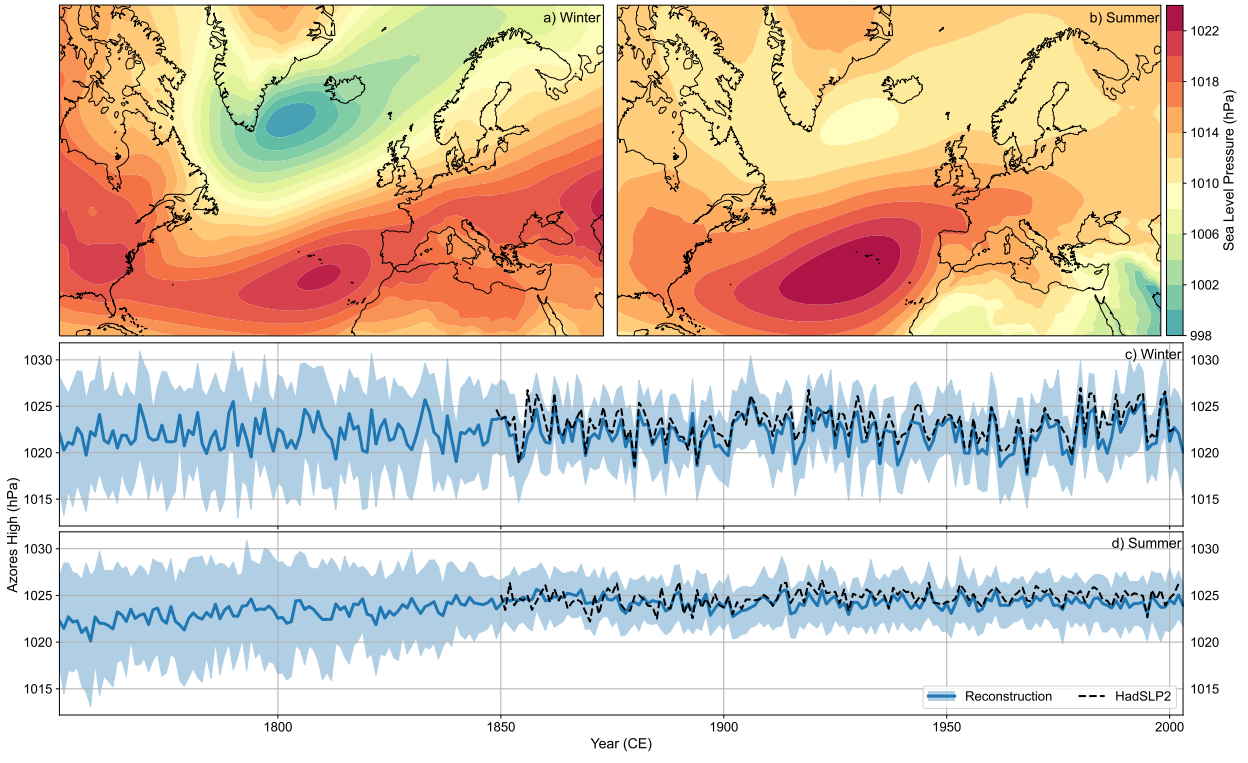

FIG. 5. SLP variability over the Azores High region from 1750 to 2004 CE. Climatological (1750-2004) mean SLP (shading, in hPa) obtained with the optimized reconstruction for: (a) winter (DJF) and (b) summer (JJA). Seasonal mean time series (1750-2004) of the intensity of the (c) winter and (d) summer Azores High (blue lines, in hPa). Shading shows the uncertainty range calculated as two standard deviations over the $5^\circ \times 5^\circ$ area where the maximum of SLP is located. Dashed lines illustrate the Azores High intensity for the HadSLP2 and the 1850-2004 period.

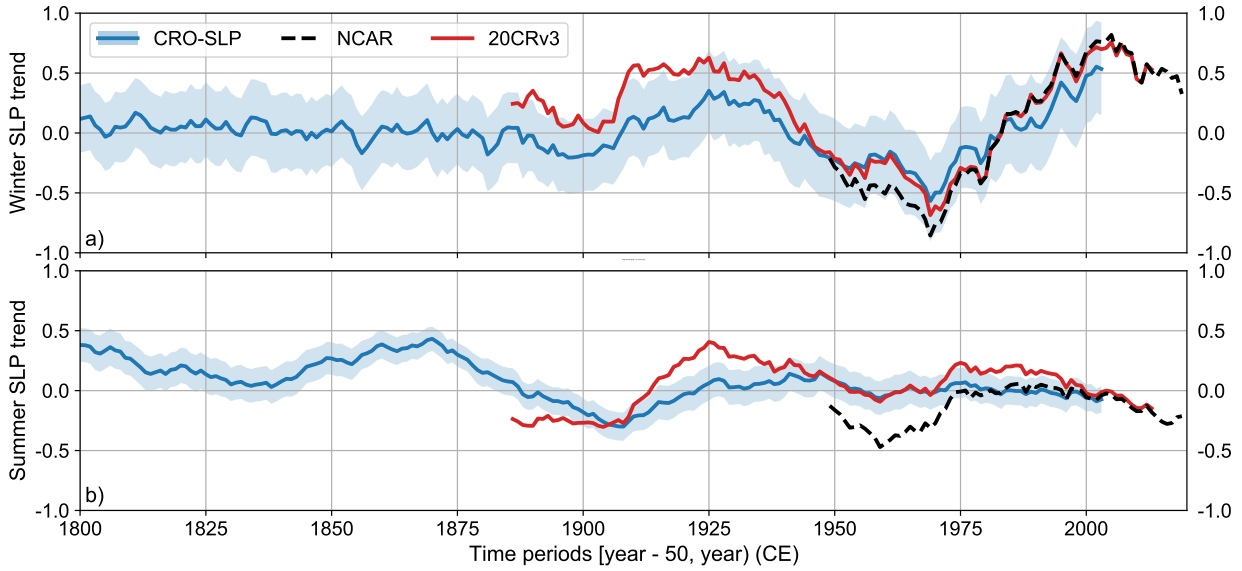

1075 FIG. 6. Decadal SLP trends of the Azores High pressure center intensity. (a) winter and (b) summer decadal
1076 SLP trends (in hPa per decade) obtained from the CRO-AM reconstruction (blue line), the 20CRv3 reanalysis
1077 (red line), and the NCAR SLP dataset (dashed line), over the Azores High center for 50-year running windows
1078 from 1750 to 2019 CE. Blue shading illustrates the uncertainty range of CRO-AM as two standard deviations
1079 with respect to the mean.

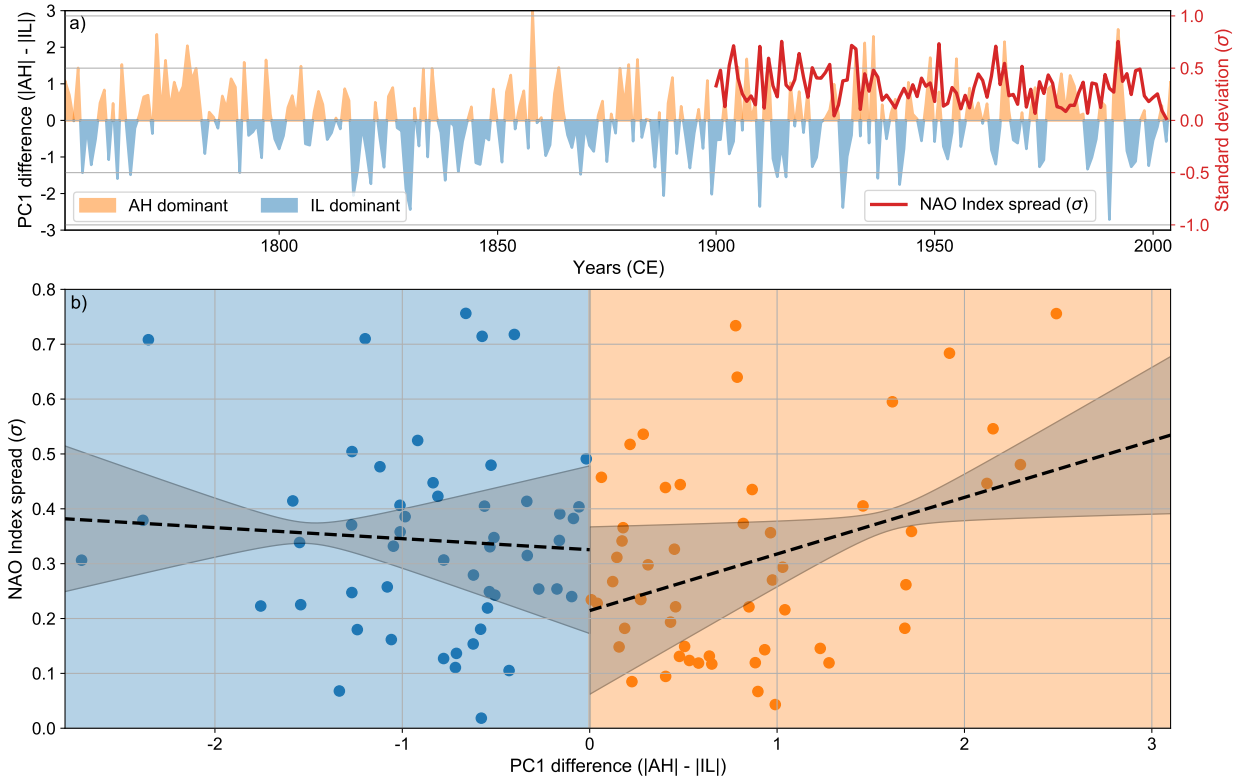

1080 FIG. 7. Contribution of the Azores High and Iceland Low to the winter NAO. (a) Time series (1751-2004) of the
1081 winter |AH|-|IL| index, denoting the unbalanced contribution of the Azores High and Iceland Low anomalies to
1082 the winter NAO. Positive (orange) and negative (blue) values show winters with a leading influence of the Azores
1083 High and Iceland Low, respectively. The red line represents the spread (standard deviation) of NAO values for
1084 each winter of the 1900-2004 period, calculated from a suite of instrumental-based NAO (Table S1). (b) Scatter
1085 plot (1900-2004) of the spread of NAO indices for winters dominated by the Iceland Low (blue section) and the
1086 Azores High (orange section). Dashed lines represent separate linear regressions for each dominant component.
1087 Grey shading shows the 95% confidence interval of the linear fits. All series have been standardized with respect
1088 to the 1951-2000 baseline.

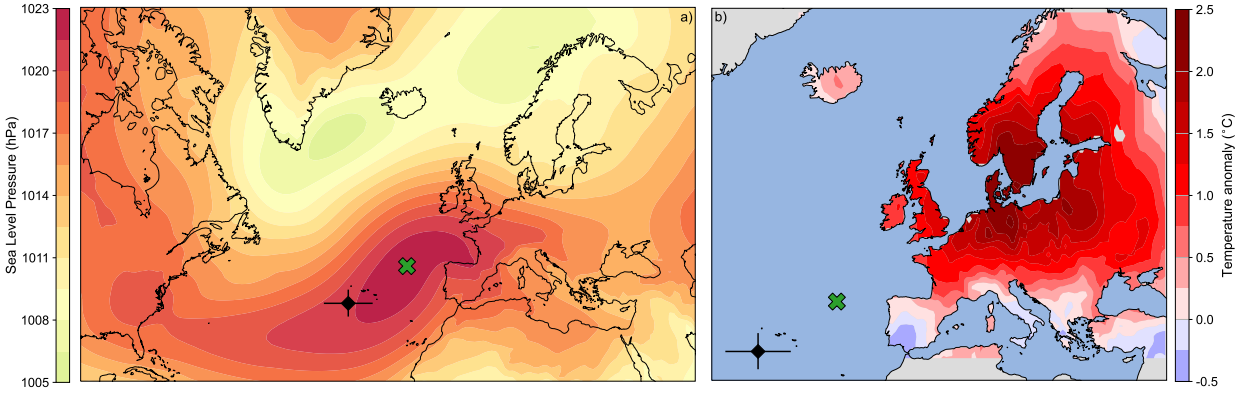

FIG. 8. Azores High shift in the extremely warm summer of 1783 CE. (a) Summer mean SLP (shading, in hPa) for 1783 obtained from the optimized reconstruction. (b) Summer mean temperature anomalies (in °C, with respect to 1500-2002) for 1783 as reconstructed by Luterbacher et al. (2004). Black diamonds with error bars show the climatological (1750-2002) location (mean and two standard deviations) of the Azores High center. Green crosses represent the center of the Azores High for the summer of 1783.

Monthly North Atlantic Sea Level Pressure reconstruction back to 1750 CE using Artificial Intelligence optimization: Supplemental Material

FERNANDO JAUME-SANTERO[1,2], DAVID BARRIOPEDRO[2], RICARDO GARCÍA-HERRERA[1,2], AND JÜRG LUTERBACHER[3]

[1] *Departamento de Ciencias de la Tierra y Astrofísica, Facultad de Ciencias Físicas, Universidad Complutense de Madrid, Madrid, Spain*
[2] *Instituto de Geociencias (IGEO), CSIC-UCM, Madrid, Spain*
[3] *Science and Innovation Department, World Meteorological Organization (WMO), Geneva, Switzerland*

1. SUPPLEMENTAL TABLES

Table S1. Definition of NAO and EA indices. All indices have been re-standardized with respect to 1951-2000.

Index	Definition	Period
	NAO	
Jones et al. (1997)	Normalized pressure difference between Azores and Iceland	1825-2014
Luterbacher et al. (2001)	Standardized SLP difference between Azores and Iceland, each region defined as the mean of 4 grid points on a 5° × 5° grid	1750-2001
Vinther et al. (2003)	Pressure observations from Cádiz/San Fernando (Gibraltar) and SW Iceland	1821-1999
Küttel et al. (2010)	Standardized SLP difference between Azores and Iceland, each region defined the mean of 4 grid points on a 5° × 5° grid	1750-2004
Hurrell and Deser, (2010)	First principal component of standardized SLP anomalies (20°-80°N, 90°W-40°E)	1899-2019
	EA	
Küttel et al. (2010)	Second principal component of standardized SLP anomalies (20°-70°N, 40°W-50°E)	1750-2004
Comas-Bru et al. (2018)	Composite of EA series generated from historical records at Bergen Florida and Valentia, and five reanalyses	1852-2014

2. SUPPLEMENTAL FIGURES

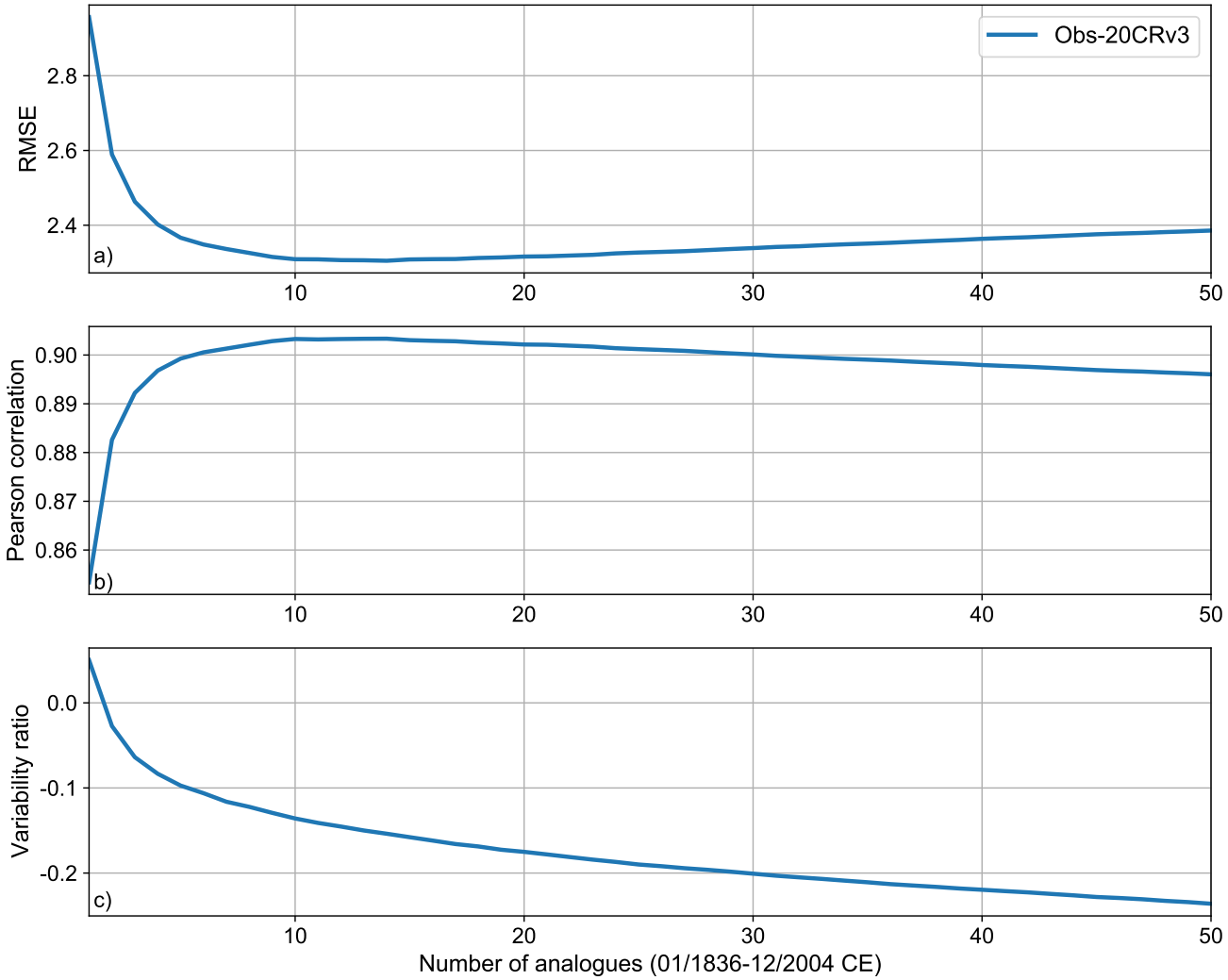

Fig. S1. Sensitivity of the reconstruction skill to the number of analogues. Panels show performance metrics of the North Atlantic SLP reconstruction for 1836-2004 (with respect to the 20CRv3) as a function of the number of analogues selected in the AM: (a) the area-weighted RMSE (in hPa); (b) the Pearson correlation coefficient; (c) the variability ratio between the reconstructed and targeted SLP field.

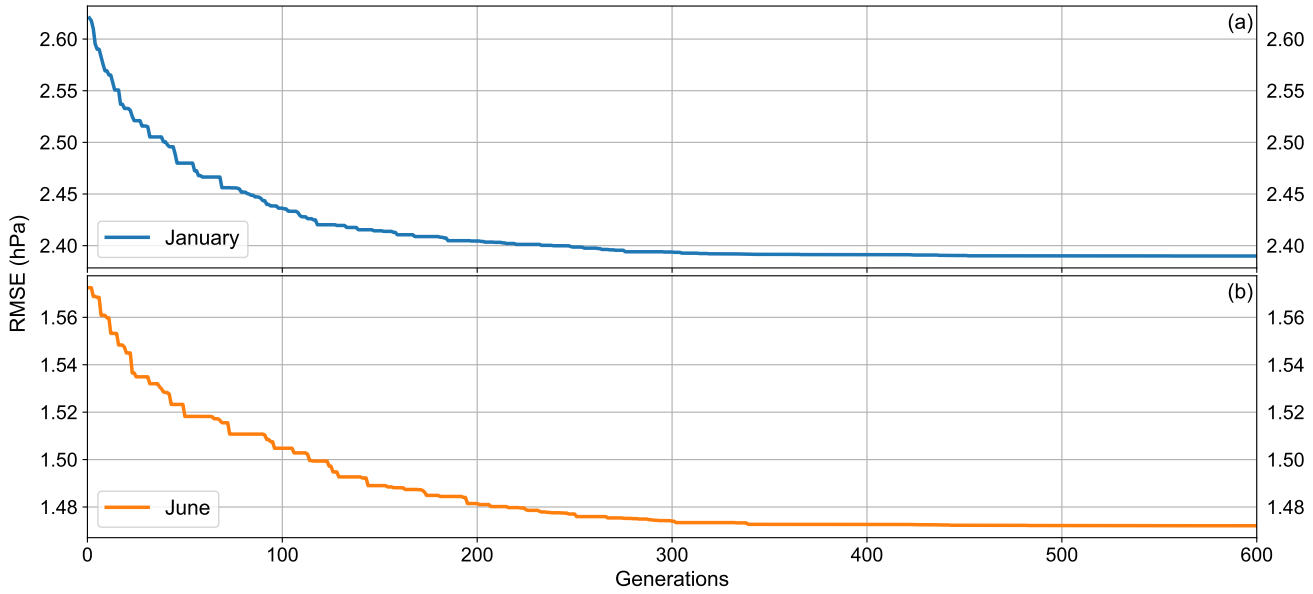

Fig. S2. CRO-AM reconstruction error of the North Atlantic SLP field over 1836-2004 (in hPa) for the month of (a) January and (b) June as a function of the number of generations (i.e., CRO iterations).

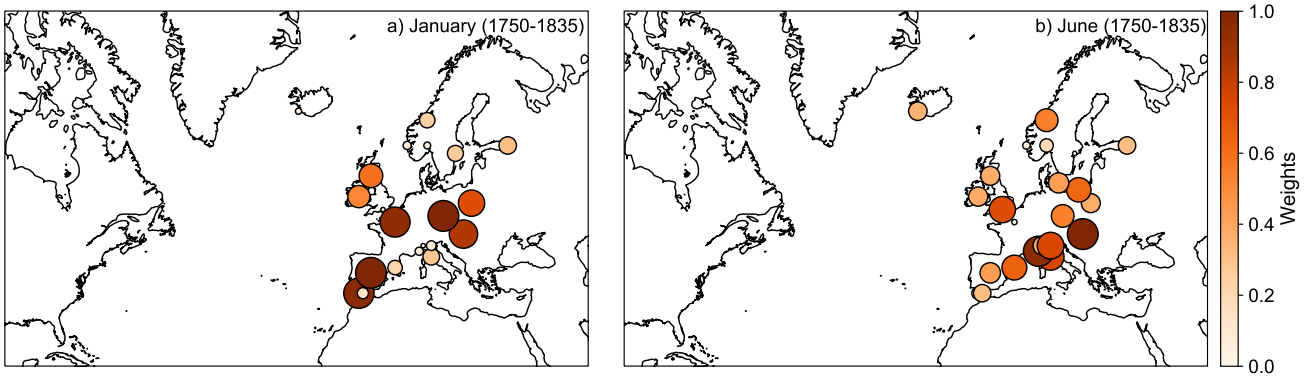

Fig. S3. As Fig. 3 but for the reanalysis experiment of the CRO-AM reconstruction. Monthly weights for (a) January and (b) June obtained with a perfect (noise free) network of SLP pseudo-observations for the period 1919-2004 taken from the 20CRv3 reanalysis with the same gaps as the real observations for the period 1750-1835.

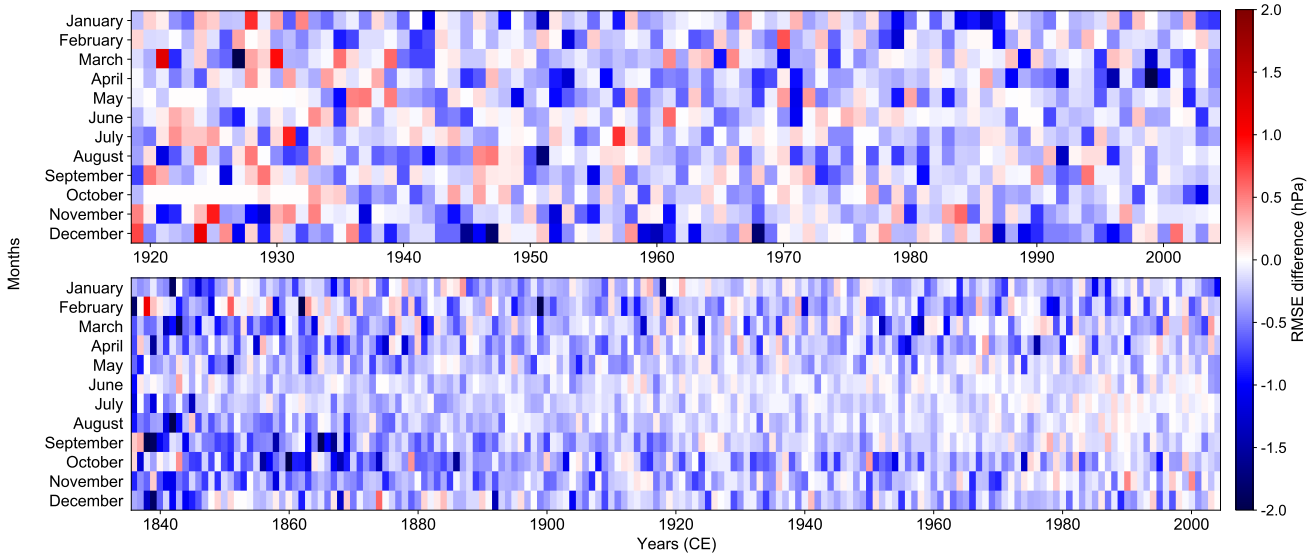

Fig. S4. Area-weighted RMSE difference between monthly SLP reconstructions generated with and without optimization of the observing network. The area-weighted RMSE of the North Atlantic SLP reconstructions generated with the observing network of 1750-1835 (1836-2004) is calculated with respect to the 1919-2004 (1836-2004) period of the 20CRv3 reanalysis, and shown in the top (bottom) panel. Blue (red) colors indicate that the optimized reconstruction has lower (higher) RMSE than its non-optimized counterpart.

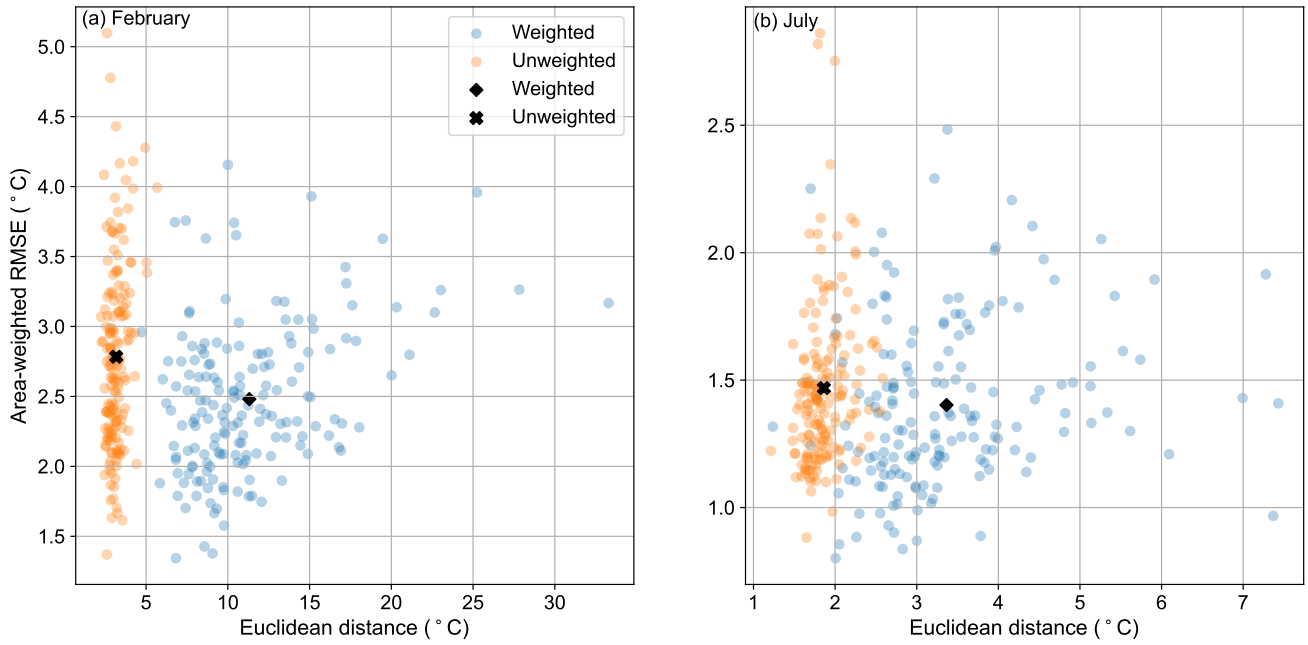

Fig. S5. Area-weighted Root Mean-Squared Error as a function of the average Euclidean distance of the 10 best analogues employed to reconstruct the months of (a) February and (b) July. Black diamonds and crosses represent the mean values of the weighted (blue dots) and un-weighted (orange dots) reconstructions from 1836 CE to 2004 CE.

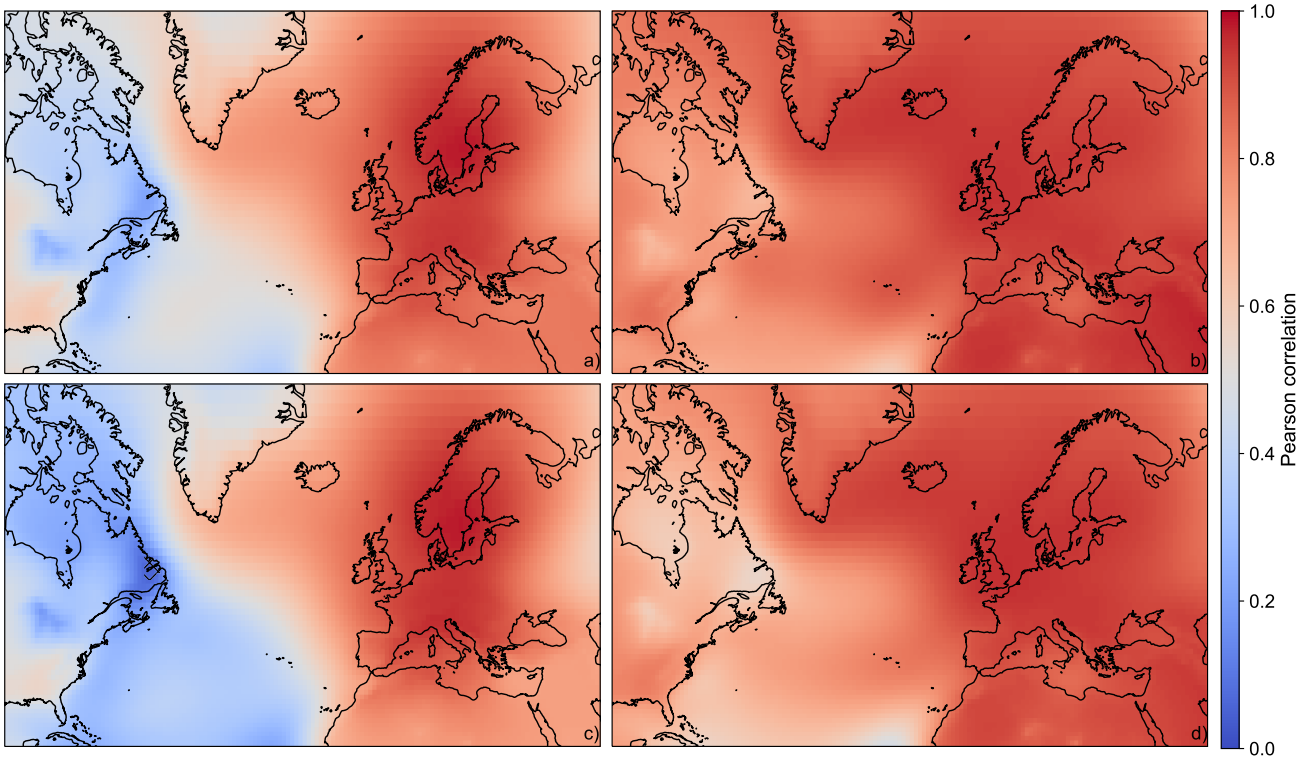

Fig. S6. Pearson correlation between SLP target fields and their optimized and non-optimized reconstructions. Pearson correlation coefficient with the 20CRv3 reanalysis between the CRO-AM (a and b) and AM (c and d) SLP reconstructions generated with the observing network of: (a and c) 1750-1835; (b and d) 1836-2004. All grid-point correlations are significant at $p < 0.05$.

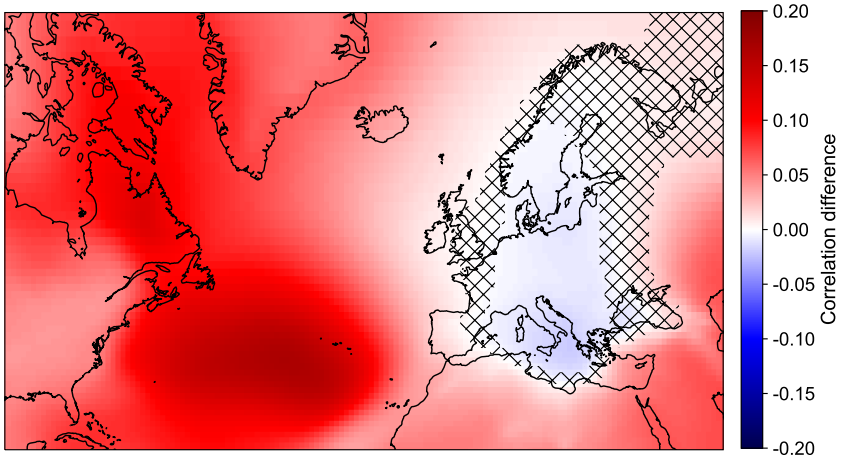

Fig. S7. As the top panels of Fig. 4 but for the SLP pseudo-reconstructions (1750-1835) of the MRI-ESM2-0 model. Shading shows the difference in performance (Pearson correlation coefficient with the 1750-1835 targeted SLP field of the MRI-ESM2-0 model) between the SLP pseudo-reconstructions generated with and without optimization of the pseudo-observing network (the simulated SLP series at the grid points matching the locations and availability of the observing network for 1750-1835).

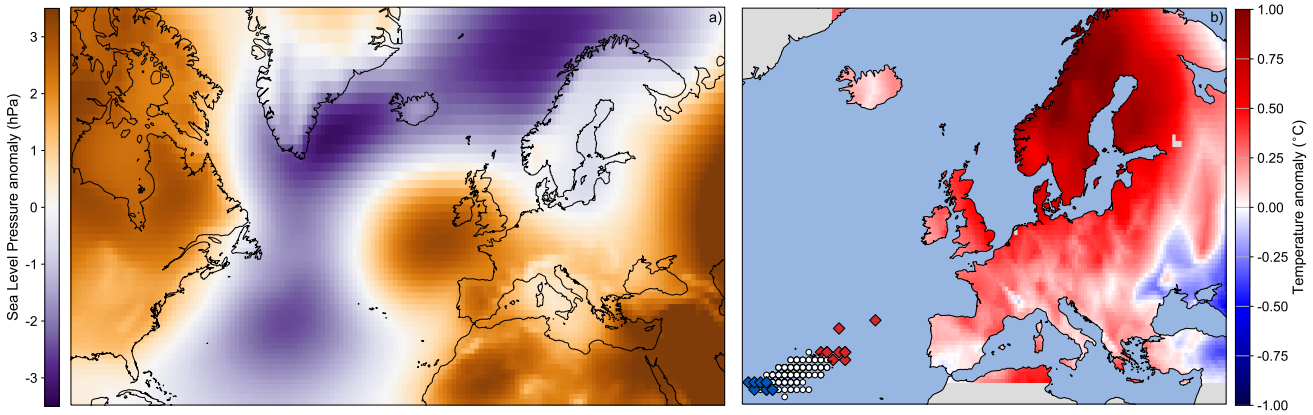

Fig. S8. SLP and temperature composite difference between the top ten northeasternmost minus top ten southwesternmost summer mean AH centers from 1750 to 2002 CE. (a) Summer mean SLP difference obtained from CRO-SLP (in hPa). (b) Summer mean temperature difference, as inferred from the reconstruction of Luterbacher et al. (2004) (in °C, with respect to 1500-2002). White dots show the climatological location of the Azores High center. Red (blue) diamonds represent the center of the Azores High for the top ten northeasternmost (southwesternmost) summers.